Commun. Comput. Phys.
doi: 10.4208/cicp.OA-2024-0145

Vol. **37**, No. 1, pp. 250-288
January 2025

Application of Gas-Kinetic Unified Algorithm for Solving Boltzmann Model Equation with Vibrational Energy Excitation

Fan Li[1], Zhi-Hui Li[1,*], Jia-Zhi Hu[1] and Wen-Qiang Hu[2]

[1] *China Aerodynamics Research and Development Center, Mianyang 621000, China.*
[2] *Beijing Institute of Space Long March Vehicle, Beijing 100076, China.*

Received 29 June 2024; Accepted (in revised version) 23 August 2024

Abstract. In recent decades, the gas-kinetic unified algorithm (GKUA) is proposed to simulate the gas flow in the whole flow regimes. In previous studies, GKUA was extended to problems of flows around the aircraft and internal flows considering the influence of rotational energy, as well as the flows around the aircraft considering the influence of vibrational energy. In this paper, we try to apply the model considering the effect of vibrational energy to the engine internal and external mixed flow problem, and build a numerical simulation framework of engine internal and external mixed flow considering the effect of vibrational energy. The reliability of the algorithm is verified by using one-dimensional shock tube problem and two-dimensional nozzle internal flow problem. The results show that the model can describe the flow problem of high temperature nozzle internal flow. Then the two-dimensional nozzle internal and external mixed flow problem of 25N attitude control engine is studied, the unsteady evolution and non-equilibrium effect of the mixed flow field are analyzed, and the flow parameter distribution of the mixed flow field without internal energy excitation, considering rotational energy excitation and considering vibrational energy excitation are compared.

AMS subject classifications: 35Q20, 76P05, 82C40

Key words: Thermodynamic non-equilibrium, Boltzmann model equation, gas-kinetic unified algorithm, aerodynamics covering various flow regimes, nozzle flow.

1 Introduction

With the gradual maturity of the mass production of recoverable vehicles and satellites, the pace of human space development has gradually accelerated, and the number of various types of spacecraft in orbit has shown an explosive growth trend. Attitude and orbit

*Corresponding author. *Email addresses:* 748867007@qq.com (F. Li), lizhihui@cardc.cn (Z.-H. Li), 17862726389@163.com (J.-Z. Hu), vincenthu@buaa.edu.cn (W.-Q. Hu)

engine reaction control system (RCS) is often used for maneuver and attitude control of space in-orbit flight and reentry vehicles [1–3]. The flow in the high-pressure air chamber at the nozzle entrance and the flow near the nozzle exit area of the attitude orbit control engine belong to continuum flow, with near-continuum flow near the nozzle exit and highly rarefied flow near the vacuum far away from the nozzle exit. The coexistence of multi-flow regimes in the same flow field due to the different degrees of rarefaction of gas poses a great challenge to the numerical simulation method.

For multi-regime flow problems, wind tunnel experiment has limitations because it cannot reproduce similar parameters such as Reynolds number, Mach number, Knudsen number, and wall temperature ratio at the same time [4]. In practice, people usually use the hybrid method [3, 5–8] and the unified method [9–13] to deal with such problems. The commonly used hybrid method is to couple the NS method with the DSMC method and realize the combination of the two methods in the transitional flow region. Since it is a coupling method in nature, both the accuracy and stability need to be considered when designing coupling ideas, and the problem of statistical fluctuation caused by DSMC method always exists. Based on the kinetic theory of gases, the unified method aims to use one method to simulate multi-scale flow problems in the whole regimes. The unified methods include unified gas-kinetic scheme (UGKS) [14–16], discrete unified gas-kinetic scheme (DUGKS) [17,18], gas-kinetic unified algorithm (GKUA) [19,20], unified stochastic particle BGK, (USP-BGK) [21] and unified gas kinetic wave-particle (UGKWP) [22,23]. In this paper, gas-kinetic unified algorithm solving multi-regime flow around problem and parallel computing application research platform for aerodynamic/thermal problems of spacecraft reentry multi-regime multi-scale flow around which are established by Li [19,20] are used to study the in-orbit spacecraft engine internal and external mixed flow problem.

Since the gas ejected from the engine is a high-temperature polyatomic mixture gas, the combustion chamber temperature is higher, and the high-temperature environment makes the internal energy of the gas medium in an excited state, which affects the gas transport coefficient and the parameter distribution of the internal and external mixed flow field of the engine. Wang et al. [24] proposed a semi-classical method for treating polyatomic gases with internal energy effects and obtained the WCU equation. Based on this, Morse [25] constructed a model equation considering the interrupted energy levels of the intramolecular energy. However, the above studies did not distinguish rotational and vibrational energy, and the internal energy was a single mode. In the case of ignoring the quantum effect in high temperature gas flow, the internal energy state of gas molecules is considered as continuous, and the classical thermodynamic method was adopted to obtain the Rykov model [26] of diatomic gas considering the influence of rotational energy. On the basis of Morse's research, Holway [27] used classical thermodynamic methods to deal with rotational energy and discontinuous energy level methods to deal with vibrational energy, and established an ES-BGK model suitable for polyatomic gases. In previous works, Peng et al. [28] used continuous energy levels to deal with rotational energy and vibrational energy, and decomposed the collision

term of the Boltzmann equation into two parts: elastic and inelastic. At the same time, the inelastic collision part is decomposed into translational-rotational energy relaxation term and translational-rotational-vibrational energy relaxation term. A class of Boltzmann model equation considering rotational energy and vibrational energy excitations are constructed. This work try to apply the model considering the effect of vibrational energy to the engine internal and external mixed flow problem, and build a numerical simulation framework of engine internal and external mixed flow considering the effect of vibrational energy. The model equation is solved under the gas-kinetic unified algorithm system, and the reliability is verified by the one-dimensional shock tube problem and the two-dimensional nozzle internal flow problem. Then the two-dimensional nozzle internal and external mixed flow problem of 25N attitude control engine is studied, and the unsteady evolution and non-equilibrium effect of the mixed flow field are analyzed. The flow field parameter distributions of the mixed flow field without considering internal energy excitation, rotational energy excitation and vibrational energy excitation are compared.

The structure of this paper is arranged as follows: Section I introduces the relevant background, and Section II introduces the computable modeling of Boltzmann equations considering vibrational energy excitation. Section III is the verification and analysis of the algorithm. The reliability of the algorithm is verified by using the one-dimensional shock tube problem and the two-dimensional nozzle internal flow problem, and the internal and external mixed flow simulation study is carried out by taking the two-dimensional nozzle of 25N attitude control engine as the object. Section IV is the conclusion.

2 The computable modeling of Boltzmann equations considering vibrational energy excitation

2.1 Gas-kinetic model equation

For polyatomic gases, the molecular energy modes include translational energy, rotational energy, and vibrational energy. By introducing the Larsen-Bergnakke phenomenological model in DSMC method, the rotational energy and vibrational energy are treated as continuously distributed energy modes, and the collision terms of Boltzmann equation are decomposed into elastic and inelastic collision terms. At the same time, the inelastic collision term is decomposed into translational-rotational energy relaxation and translational-rotational-vibrational energy relaxation according to a certain relaxation rate. The relaxation between rotational energies, vibrational energies, and rotational-vibrational energies are ignored, and the Boltzmann model equations considering vibra-

tional energy excitation are obtained in the following form:

$$\begin{cases} \dfrac{\partial f_1}{\partial t}+\boldsymbol{V}\cdot\dfrac{\partial f_1}{\partial \boldsymbol{x}}=\nu_{\rm tot}\left(f_1^{\rm t}-f_1+\dfrac{f_1^{\rm t,r}-f_1^{\rm t}}{Z_{\rm rot}}+\dfrac{f_1^{\rm t,r,v}-f_1^{\rm t}}{Z_{\rm vib}}\right), \\ \dfrac{\partial f_2}{\partial t}+\boldsymbol{V}\cdot\dfrac{\partial f_2}{\partial \boldsymbol{x}}=\nu_{\rm tot}\left(f_2^{\rm t}-f_2+\dfrac{f_2^{\rm t,r}-f_2^{\rm t}}{Z_{\rm rot}}+\dfrac{f_2^{\rm t,r,v}-f_2^{\rm t}}{Z_{\rm vib}}\right), \\ \dfrac{\partial f_3}{\partial t}+\boldsymbol{V}\cdot\dfrac{\partial f_3}{\partial \boldsymbol{x}}=\nu_{\rm tot}\left(f_3^{\rm t}-f_3+\dfrac{f_3^{\rm t,r}-f_3^{\rm t}}{Z_{\rm rot}}+\dfrac{f_3^{\rm t,r,v}-f_3^{\rm t}}{Z_{\rm vib}}\right), \end{cases} \tag{2.1}$$

where

$$f_1(t,\boldsymbol{x},\boldsymbol{V})=\int_0^{+\infty}\int_0^{+\infty} f(t,\boldsymbol{x},\boldsymbol{V};e_{\rm rot},e_{\rm vib})\,{\rm d}e_{\rm rot}{\rm d}e_{\rm vib}, \tag{2.2a}$$

$$f_2(t,\boldsymbol{x},\boldsymbol{V})=\int_0^{+\infty}\int_0^{+\infty} e_{\rm rot}f(t,\boldsymbol{x},\boldsymbol{V};e_{\rm rot},e_{\rm vib})\,{\rm d}e_{\rm rot}{\rm d}e_{\rm vib}, \tag{2.2b}$$

$$f_3(t,\boldsymbol{x},\boldsymbol{V})=\int_0^{+\infty}\int_0^{+\infty} e_{\rm vib}f(t,\boldsymbol{x},\boldsymbol{V};e_{\rm rot},e_{\rm vib})\,{\rm d}e_{\rm rot}{\rm d}e_{\rm vib}, \tag{2.2c}$$

$$f_1^{\rm t}=n\left(\frac{m}{2\pi k_{\rm B}T_{\rm t}}\right)^{3/2}\exp\left(-\frac{mC^2}{2k_{\rm B}T_{\rm t}}\right), \tag{2.2d}$$

$$f_2^{\rm t}=\frac{\delta_{\rm rot}k_{\rm B}T_{\rm r}}{2}f_1^{\rm t}, \tag{2.2e}$$

$$f_3^{\rm t}=\frac{\delta_{\rm vib}(T_{\rm v})k_{\rm B}T_{\rm v}}{2}f_1^{\rm t}, \tag{2.2f}$$

$$f_1^{\rm t,r}=n\left(\frac{m}{2\pi k_{\rm B}T^{\rm t,r}}\right)^{3/2}\exp\left(-\frac{mC^2}{2k_{\rm B}T^{\rm t,r}}\right), \tag{2.2g}$$

$$f_2^{\rm t,r}=\frac{\delta_{\rm rot}k_{\rm B}T^{\rm t,r}}{2}f_1^{\rm t,r}, \tag{2.2h}$$

$$f_3^{\rm t,r}=\frac{\delta_{\rm vib}(T_{\rm v})k_{\rm B}T_{\rm v}}{2}f_1^{\rm t,r}, \tag{2.2i}$$

$$f_1^{\rm t,r,v}=n\left(\frac{m}{2\pi k_{\rm B}T^{\rm t,r,v}}\right)^{3/2}\exp\left(-\frac{mC^2}{2k_{\rm B}T^{\rm t,r,v}}\right), \tag{2.2j}$$

$$f_2^{\rm t,r,v}=\frac{\delta_{\rm rot}k_{\rm B}T^{\rm t,r,v}}{2}f_1^{\rm t,r,v}, \tag{2.2k}$$

$$f_3^{\rm t,r,v}=\frac{\delta_{\rm vib}(T^{\rm t,r,v})k_{\rm B}T^{\rm t,r,v}}{2}f_1^{\rm t,r,v}, \tag{2.2l}$$

$$\nu_{\rm tot}=Pr\cdot nk_{\rm B}\frac{T_{\rm t}}{\mu}. \tag{2.2m}$$

Here, t is the time, $\boldsymbol{x}$ is the spatial position coordinate, $\boldsymbol{V}$ is the molecular motion velocity, $f(t,\boldsymbol{x},\boldsymbol{V};e_{\rm rot},e_{\rm vib})$ is the velocity distribution function of gas molecules with rotational

and vibrational energies, $e_{\rm rot}$ and $e_{\rm vib}$ are rotational and vibrational modulus respectively, f_1, f_2 and f_3 are the reduced molecular velocity distribution functions corresponding to translational, rotational and vibrational energies, $Z_{\rm rot}$ and $Z_{\rm vib}$ are the number of rotational and vibrational relaxation collisions, $\nu_{\rm tot}$ is the total collision frequency. Pr is the gas Prandtl number and μ is the gas viscosity coefficient. $f_i^{\rm t}$ is the velocity distribution function of gas molecules characterizing the relaxation of elastic collisions, $f_i^{\rm t,r}$ is the velocity distribution function characterizing the relaxation of translational-rotational energy in inelastic collisions, $f_i^{\rm t,r,v}$ is the velocity distribution function characterizing the relaxation of translational-rotational-vibrational energy in inelastic collisions. $T_{\rm t}$, $T_{\rm r}$ and $T_{\rm v}$ are the translational temperature, rotational temperature and vibration temperature, respectively. $T^{\rm t,r}$ and $T^{\rm t,r,v}$ are the translational-rotational effective temperature and the translational-rotational-vibrational effective temperature, respectively. $k_{\rm B}$ is Boltzmann constant, $\delta_{\rm rot}$ and $\delta_{\rm vib}$ are rotational and vibrational degrees of freedom, respectively.

Since the rotational characteristic temperature $\Theta_{\rm rot}$ of gas is very low, it is generally assumed that $\delta_{\rm rot}=2$ for linear molecules such as oxygen molecules, nitrogen molecules, carbon dioxide molecules, etc., and $\delta_{\rm rot}=3$ for nonlinear molecules such as water molecules, etc. The characteristic temperature $\Theta_{\rm vib}$ of water molecules is high (for example, oxygen is 2256K, nitrogen is 3371K), and the vibration energy is difficult to be fully excited in general. The vibration degree of freedom $\delta_{\rm vib}$ is a function of temperature, and its expression is:

$$\delta_{\rm vib}(T)=2\sum_{i=1}^{N}\frac{\Theta_{\rm vib,i}/T}{\exp(\Theta_{\rm vib,i}/T)-1}. \tag{2.3}$$

Here, N is the vibrational energy mode of the gas molecule, M is the number of atoms in the molecule, for linear molecules $N=3M-5$, for nonlinear molecules $N=3M-6$, $\Theta_{\rm vib,i}$ is the vibrational characteristic temperature in the i-th vibrational energy mode.

The translational-rotational effective temperature $T^{\rm t,r}$ and the translational-rotational-vibrational effective temperature $T^{\rm t,r,v}$ can be defined as follows:

$$T^{\rm t,r}=\frac{3T_{\rm t}+\delta_{\rm rot}T_{\rm r}}{3+\delta_{\rm rot}}, \tag{2.4}$$

$$T^{\rm t,r,v}=\frac{3T_{\rm t}+\delta_{\rm rot}T_{\rm r}+\delta_{\rm vib}(T_{\rm v})T_{\rm v}}{3+\delta_{\rm rot}+\delta_{\rm vib}(T^{\rm t,r,v})}. \tag{2.5}$$

At any time, according to the velocity distribution function, the expression of macroscopic flow can be obtained as follows:

$$n=\int_{-\infty}^{+\infty}f_1{\rm d}\boldsymbol{V}, \tag{2.6a}$$

$$n\boldsymbol{U}=\int_{-\infty}^{+\infty}\boldsymbol{V}f_1{\rm d}\boldsymbol{V}, \tag{2.6b}$$

$$\frac{3k_{\rm B}T_{\rm t}}{2}=\frac{m}{2n}\int_{-\infty}^{+\infty}C^2f_1{\rm d}\boldsymbol{V}, \tag{2.6c}$$

$$\frac{\delta_{\rm rot} n k_{\rm B} T_{\rm r}}{2} = \int_{-\infty}^{+\infty} f_2 {\rm d}\boldsymbol{V}, \tag{2.6d}$$

$$\frac{\delta_{\rm vib}(T_{\rm v}) n k_{\rm B} T_{\rm v}}{2} = \int_{-\infty}^{+\infty} f_3 {\rm d}\boldsymbol{V}, \tag{2.6e}$$

$$\tau_{ij} = m \int_{-\infty}^{+\infty} C_i C_j f_1 {\rm d}\boldsymbol{V}, \tag{2.6f}$$

$$p_{\rm t} = n k_{\rm B} T_{\rm t}, \tag{2.6g}$$

$$q_{\rm t} = \frac{m}{2} \int_{-\infty}^{+\infty} \boldsymbol{C} C^2 f_1 {\rm d}\boldsymbol{V}, \tag{2.6h}$$

$$q_{\rm r} = \int_{-\infty}^{+\infty} \boldsymbol{C} f_2 {\rm d}\boldsymbol{V}, \tag{2.6i}$$

$$q_{\rm v} = \int_{-\infty}^{+\infty} \boldsymbol{C} f_3 {\rm d}\boldsymbol{V}, \tag{2.6j}$$

where n is the number density, $\boldsymbol{U}$ is the macroscopic flow velocity, m is the molecular mass, τ is the stress tensor, $p_{\rm t}$ is the pressure, $\boldsymbol{q}$ is the heat flux vector, and $\boldsymbol{C}$ is the random thermal motion velocity of molecules, which is defined as $\boldsymbol{C} = \boldsymbol{V} - \boldsymbol{U}$.

2.2 Dimensionless processing of gas-kinetic model equation

For the convenience of numerical solution, the following dimensionless parameters are introduced to make gas-kinetic model equation model dimensionless:

$$f_{1\infty} = \frac{n_\infty}{C_{m\infty}^3}, \quad f_{2\infty} = \frac{n_\infty k_{\rm B} T_\infty}{C_{m\infty}^3}, \quad f_{3\infty} = \frac{n_\infty k_{\rm B} T_\infty}{C_{m\infty}^3}, \tag{2.7}$$

$$C_{m\infty} = \sqrt{\frac{2 k_{\rm B} T_\infty}{m}}, q_\infty = n_\infty k_{\rm B} T_\infty C_{m\infty}. \tag{2.8}$$

Then the governing equation can be written as follows:

$$\begin{cases} \dfrac{\partial \widetilde{f}_1}{\partial \widetilde{t}} + \widetilde{\boldsymbol{V}} \cdot \dfrac{\partial \widetilde{f}_1}{\partial \widetilde{\boldsymbol{x}}} = \widetilde{\nu}_{\rm tot} \left(\widetilde{f}_1^{\rm t} - \widetilde{f}_1 + \dfrac{\widetilde{f}_1^{\rm t,r} - \widetilde{f}_1^{\rm t}}{Z_{\rm rot}} + \dfrac{\widetilde{f}_1^{\rm t,r,v} - \widetilde{f}_1^{\rm t}}{Z_{\rm vib}} \right), \\ \dfrac{\partial \widetilde{f}_2}{\partial \widetilde{t}} + \widetilde{\boldsymbol{V}} \cdot \dfrac{\partial \widetilde{f}_2}{\partial \widetilde{\boldsymbol{x}}} = \widetilde{\nu}_{\rm tot} \left(\widetilde{f}_2^{\rm t} - \widetilde{f}_2 + \dfrac{\widetilde{f}_2^{\rm t,r} - \widetilde{f}_2^{\rm t}}{Z_{\rm rot}} + \dfrac{\widetilde{f}_2^{\rm t,r,v} - \widetilde{f}_2^{\rm t}}{Z_{\rm vib}} \right), \\ \dfrac{\partial \widetilde{f}_3}{\partial \widetilde{t}} + \widetilde{\boldsymbol{V}} \cdot \dfrac{\partial \widetilde{f}_3}{\partial \widetilde{\boldsymbol{x}}} = \widetilde{\nu}_{\rm tot} \left(\widetilde{f}_3^{\rm t} - \widetilde{f}_3 + \dfrac{\widetilde{f}_3^{\rm t,r} - \widetilde{f}_3^{\rm t}}{Z_{\rm rot}} + \dfrac{\widetilde{f}_3^{\rm t,r,v} - \widetilde{f}_3^{\rm t}}{Z_{\rm vib}} \right), \end{cases} \tag{2.9}$$

$$\widetilde{f}_1^{\mathrm{t}}=\widetilde{n}\left(\frac{1}{\pi\widetilde{T}_{\mathrm{t}}}\right)^{3/2}\exp\left(-\frac{\widetilde{C}^2}{\widetilde{T}_{\mathrm{t}}}\right), \tag{2.10a}$$

$$\widetilde{f}_2^{\mathrm{t}}=\frac{\delta_{\mathrm{rot}}\widetilde{T}_{\mathrm{r}}}{2}\widetilde{f}_1^{\mathrm{t}}, \tag{2.10b}$$

$$\widetilde{f}_3^{\mathrm{t}}=\frac{\delta_{\mathrm{vib}}(T_{\mathrm{v}})\widetilde{T}_{\mathrm{v}}}{2}\widetilde{f}_1^{\mathrm{t}}, \tag{2.10c}$$

$$\widetilde{f}_1^{\mathrm{t,r}}=\widetilde{n}\left(\frac{1}{\pi\widetilde{T}^{\mathrm{t,r}}}\right)^{3/2}\exp\left(-\frac{\widetilde{C}^2}{\widetilde{T}^{\mathrm{t,r}}}\right), \tag{2.10d}$$

$$\widetilde{f}_2^{\mathrm{t,r}}=\frac{\delta_{\mathrm{rot}}\widetilde{T}^{\mathrm{t,r}}}{2}\widetilde{f}_1^{\mathrm{t,r}}, \tag{2.10e}$$

$$\widetilde{f}_3^{\mathrm{t,r}}=\frac{\delta_{\mathrm{vib}}(T_{\mathrm{v}})\widetilde{T}_{\mathrm{v}}}{2}\widetilde{f}_1^{\mathrm{t,r}}, \tag{2.10f}$$

$$\widetilde{f}_1^{\mathrm{t,r,v}}=\widetilde{n}\left(\frac{1}{\pi\widetilde{T}^{\mathrm{t,r,v}}}\right)^{3/2}\exp\left(-\frac{\widetilde{C}^2}{\widetilde{T}^{\mathrm{t,r,v}}}\right), \tag{2.10g}$$

$$\widetilde{f}_2^{\mathrm{t,r,v}}=\frac{\delta_{\mathrm{rot}}\widetilde{T}^{\mathrm{t,r,v}}}{2}\widetilde{f}_1^{\mathrm{t,r,v}}, \tag{2.10h}$$

$$\widetilde{f}_3^{\mathrm{t,r,v}}=\frac{\delta_{\mathrm{vib}}(T^{\mathrm{t,r,v}})\widetilde{T}^{\mathrm{t,r,v}}}{2}\widetilde{f}_1^{\mathrm{t,r,v}}, \tag{2.10i}$$

$$\widetilde{\nu}_{\mathrm{tot}}=Pr\cdot\widetilde{n}\widetilde{T}_{\mathrm{t}}^{1-\omega}\cdot\frac{2\alpha(5-2\omega)(7-2\omega)}{5(\alpha+1)(\alpha+2)\sqrt{\pi}Kn}. \tag{2.10j}$$

The expression for the macroscopic flow can be written as follows:

$$\widetilde{n}=\int_{-\infty}^{+\infty}\widetilde{f}_1\mathrm{d}\widetilde{\boldsymbol{V}}, \tag{2.11a}$$

$$\widetilde{n}\widetilde{\boldsymbol{U}}=\int_{-\infty}^{+\infty}\widetilde{\boldsymbol{V}}\widetilde{f}_1\mathrm{d}\widetilde{\boldsymbol{V}}, \tag{2.11b}$$

$$\frac{3\widetilde{T}_{\mathrm{t}}}{2}=\frac{1}{\widetilde{n}}\int_{-\infty}^{+\infty}\widetilde{C}^2\widetilde{f}_1\mathrm{d}\widetilde{\boldsymbol{V}}, \tag{2.11c}$$

$$\frac{\delta_{\mathrm{rot}}\widetilde{n}\widetilde{T}_{\mathrm{r}}}{2}=\int_{-\infty}^{+\infty}\widetilde{f}_2\mathrm{d}\widetilde{\boldsymbol{V}}, \tag{2.11d}$$

$$\frac{\delta_{\mathrm{vib}}(T_{\mathrm{v}})\widetilde{n}\widetilde{T}_{\mathrm{v}}}{2}=\int_{-\infty}^{+\infty}\widetilde{f}_3\mathrm{d}\widetilde{\boldsymbol{V}}, \tag{2.11e}$$

$$\widetilde{\tau}_{ij}=2\int_{-\infty}^{+\infty}\widetilde{C}_i\widetilde{C}_j\widetilde{f}_1\mathrm{d}\widetilde{\boldsymbol{V}}, \tag{2.11f}$$

$$\widetilde{p}_{\mathrm{t}}=\widetilde{n}\widetilde{T}_{\mathrm{t}}, \tag{2.11g}$$

$$\widetilde{q}_{\mathrm{t}}=\int_{-\infty}^{+\infty}\widetilde{\boldsymbol{C}}\widetilde{C}^2\widetilde{f}_1\mathrm{d}\widetilde{\boldsymbol{V}}, \tag{2.11h}$$

$$\widetilde{q}_{\mathrm{r}}=\int_{-\infty}^{+\infty}\widetilde{C}\widetilde{f}_2\mathrm{d}\widetilde{V}, \tag{2.11i}$$

$$\widetilde{q}_{\mathrm{v}}=\int_{-\infty}^{+\infty}\widetilde{C}\widetilde{f}_3\mathrm{d}\widetilde{V}. \tag{2.11j}$$

2.3 Gas-kinetic unified algorithm

After determining gas-kinetic model equations, discrete velocity coordinate method, unsteady time splitting method and finite difference method are used to solve the equations.

Taking two-dimensional gas flow as an example, the general formula of the computational plane Boltzmann model equation of discrete velocity space dimension reduction at discrete velocity coordinate points $(\widetilde{V}_{x\sigma},\widetilde{V}_{y\delta})$ by the discrete velocity coordinate method can be expressed as:

$$\frac{\partial\widetilde{\boldsymbol{Q}}}{\partial\widetilde{t}}+\frac{\partial\widetilde{\boldsymbol{F}}}{\partial\zeta}+\frac{\partial\widetilde{\boldsymbol{G}}}{\partial\eta}=\widetilde{\boldsymbol{S}}, \tag{2.12}$$

where

$$\widetilde{\boldsymbol{Q}}=\widetilde{\boldsymbol{J}}\begin{pmatrix}\widetilde{f}_{1\sigma,\delta}\\ \widetilde{f}_{2\sigma,\delta}\\ \widetilde{f}_{3\sigma,\delta}\end{pmatrix},\quad \widetilde{\boldsymbol{F}}=\widetilde{U}_x\widetilde{\boldsymbol{Q}},\quad \widetilde{\boldsymbol{G}}=\widetilde{U}_y\widetilde{\boldsymbol{Q}}, \tag{2.13}$$

$$\widetilde{\boldsymbol{S}}=\widetilde{\boldsymbol{J}}\begin{pmatrix}\widetilde{\nu}_{\mathrm{tot}}\left(\widetilde{f}^{\mathrm{t}}_{1\sigma,\delta}-\widetilde{f}_{1\sigma,\delta}+\frac{\widetilde{f}^{\mathrm{t,r}}_{1\sigma,\delta}-\widetilde{f}^{\mathrm{t}}_{1\sigma,\delta}}{Z_{\mathrm{rot}}}+\frac{\widetilde{f}^{\mathrm{t,r,v}}_{1\sigma,\delta}-\widetilde{f}^{\mathrm{t}}_{1\sigma,\delta}}{Z_{\mathrm{vib}}}\right)\\ \widetilde{\nu}_{\mathrm{tot}}\left(\widetilde{f}^{\mathrm{t}}_{2\sigma,\delta}-\widetilde{f}_{2\sigma,\delta}+\frac{\widetilde{f}^{\mathrm{t,r}}_{2\sigma,\delta}-\widetilde{f}^{\mathrm{t}}_{2\sigma,\delta}}{Z_{\mathrm{rot}}}+\frac{\widetilde{f}^{\mathrm{t,r,v}}_{2\sigma,\delta}-\widetilde{f}^{\mathrm{t}}_{2\sigma,\delta}}{Z_{\mathrm{vib}}}\right)\\ \widetilde{\nu}_{\mathrm{tot}}\left(\widetilde{f}^{\mathrm{t}}_{3\sigma,\delta}-\widetilde{f}_{3\sigma,\delta}+\frac{\widetilde{f}^{\mathrm{t,r}}_{3\sigma,\delta}-\widetilde{f}^{\mathrm{t}}_{3\sigma,\delta}}{Z_{\mathrm{rot}}}+\frac{\widetilde{f}^{\mathrm{t,r,v}}_{3\sigma,\delta}-\widetilde{f}^{\mathrm{t}}_{3\sigma,\delta}}{Z_{\mathrm{vib}}}\right)\end{pmatrix}. \tag{2.14}$$

$\widetilde{\boldsymbol{J}}=\frac{\partial(\widetilde{x},\widetilde{y})}{\partial(\zeta,\eta)}$ is the Jacobian matrix of the grid transformation, and the inverse molecular transformation velocity is:

$$\widetilde{U}_x=\widetilde{V}_{x\sigma}\cdot\widetilde{\zeta}_x+\widetilde{V}_{y\delta}\cdot\widetilde{\zeta}_y,\quad \widetilde{U}_y=\widetilde{V}_{x\sigma}\cdot\widetilde{\eta}_x+\widetilde{V}_{y\delta}\cdot\widetilde{\eta}_y. \tag{2.15}$$

Using the unsteady time splitting method, gas-kinetic model equation (2.12) is divided into the convective motion equation and the collision relaxation source term equation for coupling solution.

$$\frac{\partial\widetilde{\boldsymbol{Q}}}{\partial\widetilde{t}}=\widetilde{\boldsymbol{S}}, \tag{2.16a}$$

$$\frac{\partial\widetilde{\boldsymbol{Q}}}{\partial\widetilde{t}}+\frac{\partial\widetilde{\boldsymbol{F}}}{\partial\zeta}=0, \tag{2.16b}$$

$$\frac{\partial\widetilde{\boldsymbol{Q}}}{\partial\widetilde{t}}+\frac{\partial\widetilde{\boldsymbol{G}}}{\partial\eta}=0. \tag{2.16c}$$

The second-order Runge-Kutta method is used to numerically solve the collision relaxation source term equation, and the NND-4(a) numerical scheme is used to discretized the convective motion equation. Finally, the following finite difference numerical scheme is obtained:

$$\widetilde{Q}^{n+1}=L_s\left(\frac{\Delta\widetilde{t}}{2}\right)L_\eta\left(\frac{\Delta\widetilde{t}}{2}\right)L_\zeta\left(\Delta\widetilde{t}\right)L_\eta\left(\frac{\Delta\widetilde{t}}{2}\right)L_s\left(\frac{\Delta\widetilde{t}}{2}\right)\widetilde{Q}^n, \tag{2.17}$$

where L_s, L_η, and L_ζ denote the difference operators of collision relaxation source term and convective equations of motion.

The time step is given by the format stability condition:

$$\Delta\widetilde{t}=CFL/\max\left(\frac{\widetilde{\nu}_{\text{tot}}}{2},\frac{\left|\widetilde{\widetilde{U}}_x\right|}{\Delta\zeta},\frac{\left|\widetilde{\widetilde{U}}_y\right|}{\Delta\eta}\right), \tag{2.18}$$

where CFL is the time step adjustment coefficient, which is taken to be 0.95.

2.4 Numerical treatment of boundary conditions

On the wall boundary, gas molecules are reflected from the wall into the flow field. Assuming that there is no adsorption of molecules on the wall, and the reflection is instantaneous, the reflected molecules are treated as complete diffuse reflection, that is, scattering with a equilibrium distribution fully adapted to the wall temperature $\widetilde{T}_{\text{w}}$ and velocity $\widetilde{U}_{\text{w}}$, and its distribution function is:

$$\widetilde{f}_{1\text{w}}^{+}=\widetilde{n}_{\text{w}}\left(\frac{1}{\pi\widetilde{T}_{\text{w}}}\right)^{3/2}\exp\left(-\frac{\widetilde{C}_{\text{w}}^2}{\widetilde{T}_{\text{w}}}\right),\quad \widetilde{f}_{2\text{w}}^{+}=\frac{\delta_{\text{rot}}\widetilde{T}_{\text{w}}}{2}\widetilde{f}_{1\text{w}}^{+},\quad \widetilde{f}_{3\text{w}}^{+}=\frac{\delta_{\text{vib}}\left(\widetilde{T}_{\text{w}}\right)\widetilde{T}_{\text{w}}}{2}\widetilde{f}_{1\text{w}}^{+}, \tag{2.19}$$

where $\widetilde{\boldsymbol{C}}_{\text{w}}=\widetilde{\boldsymbol{V}}-\widetilde{\boldsymbol{U}}_{\text{w}}$, for a fixed wall, $\widetilde{\boldsymbol{U}}_{\text{w}}=0$, and $\widetilde{n}_{\text{w}}$ is the number density of reflected molecules on the wall. Along the normal direction of the wall, the mass flow rate of the fluid is zero, which has the following relationship:

$$\int_{-\infty,\widetilde{C}_{v\text{w}}>0}^{+\infty}\widetilde{C}_{v\text{w}}\widetilde{f}_{1\text{w}}^{+}\text{d}\widetilde{\boldsymbol{V}}+\int_{-\infty,\widetilde{C}_{v\text{w}}<0}^{+\infty}\widetilde{C}_{v\text{w}}\widetilde{f}_{1\text{w}}^{-}\text{d}\widetilde{\boldsymbol{V}}=0. \tag{2.20}$$

The number density $\widetilde{n}_{\text{w}}$ of gas molecules reflected from the wall can be obtained, where $\widetilde{C}_{v\text{w}}=\widetilde{\boldsymbol{C}}_{\text{w}}\cdot\widetilde{\boldsymbol{v}}_{\text{wall}}$, $\widetilde{\boldsymbol{v}}_{\text{wall}}$ is the normal vector outside the wall pointing to the interior of the fluid, and $\widetilde{f}_{1\text{w}}^{-}$ can be interpolated from the internal field distribution function.

For the inlet boundary, when molecules flow outwards from the flow field, the outlet data is obtained by linear extrapolation of internal field data; when molecules enter the flow field, it is taken as the equilibrium distribution function under given macroscopic flow parameter conditions. For the outlet boundary, when molecules flow outwards from the flow field, the outlet data is obtained by linear extrapolation of internal field data; when molecules enter the flow field, it is assumed that the distribution function no longer varies with position or there are no gradients in the region.

3 Numerical verification and analysis

In order to verify the reliability and accuracy of the model and algorithm, the one-dimensional shock tube problem and the two-dimensional nozzle internal flow problem are tested in this paper, and the two-dimensional nozzle internal and external mixed flow problem of 25N attitude control engine is studied. The unsteady evolution and the non-equilibrium effect of the mixed flow field are analyzed. The flow field parameter distributions of the mixed flow field without considering internal energy excitation, rotational energy excitation and vibrational energy excitation are compared.

3.1 One-dimensional shock tube problem

In order to verify the proposed vibrational energy relaxation model for polyatomic gases, the rotational relaxation collision number $Z_{\rm rot}$ and the vibrational relaxation collision number $Z_{\rm vib}$ can be set to infinity, and their numerical solutions can be taken as the limiting solutions for monatomic gases. The one-dimensional shock tube problem is used for testing, the dimensionless computational domain (the dimensionless parameter omits the top mark "$\sim$") is $x\in[0,1]$, characteristic length is defined as 1800 times the mean free path, and the reference temperature is 1000K. In the space, 500 cells with uniform mesh are used. In the particle velocity space, 200 points with uniform distribution are used. The density, velocity and temperature of gas molecules in the shock tube at the initial time are:

$$\begin{aligned} &n_{\rm L}=1.0, U_{\rm L}=0.0, \quad T_{\rm t,L}=T_{\rm r,L}=T_{\rm v,L}=2.0, \quad x\leq 0.5,\\ &n_{\rm R}=0.125, U_{\rm R}=0.0, \quad T_{\rm t,R}=T_{\rm r,R}=T_{\rm v,R}=1.6, \quad x>0.5. \end{aligned}$$

For convenience, the GKUA model with vibrational energy relaxation is denoted below by GKUA_Vib. As shown in (a), (b), and (c) in Fig. 1, when $Z_{\rm rot}\to\infty$ and $Z_{\rm vib}\to\infty$, the solutions of the Shakhov model for monatomic gas and the GKUA_Vib model for polyatomic gas are almost identical. It can be seen from Fig. 1(d) that the rotational temperature and vibrational temperature of the left and right sides of the shock tube are smoothly transitional connected. The reason is that when $Z_{\rm rot}\to\infty$ and $Z_{\rm vib}\to\infty$, it means that the average number of collisions of each gas molecule required for the system to reach the equilibrium state is infinite, and the rotational energy and vibrational energy of gas molecules do not participate in the energy conversion and are in the frozen state. Both the GKUA_Vib model and the Shakhov model use $Z_{\rm rot}\to\infty$ and $Z_{\rm vib}\to\infty$ to simulate the monatomic gas flow, which also means that the monatomic gas flow belongs to the energy freezing flow. Fig. 2 shows the distribution of physical parameters of the shock tube flow field along the x direction at the time $t=0.1912$ when $Z_{\rm rot}=3$ and $Z_{\rm vib}=30$. As can be seen in Fig. 2, when the vibrational energy excitation is considered, part of the vibrational energy is converted into rotational and translational energy, leading to an increase in rotational and translational temperatures and a faster gas velocity, while the thermodynamic nonequilibrium effect is intensified and the shock wave becomes thicker.

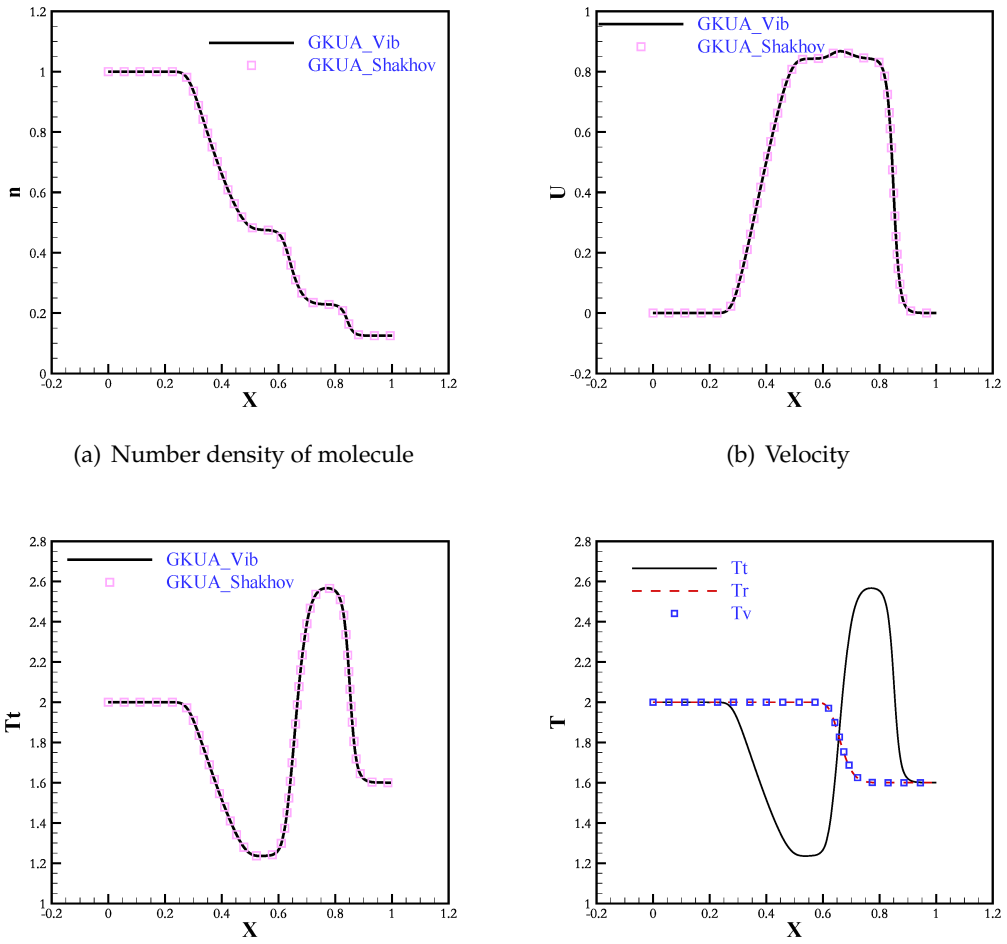

(a) Number density of molecule

(b) Velocity

(c) Translational temperature

(d) Temperature

Figure 1: Distribution of shock tube flow parameters $(Z_{\rm rot}\to\infty, Z_{\rm vib}\to\infty)$.

3.2 Two-dimensional nozzle internal flow problem

Fig. 3 shows the schematic diagram of the micronozzle structure, where $L_{\rm in}$, $L_{\rm t}$ and $L_{\rm out}$ correspond to the height of the inlet, throat and outlet of the micronozzle, respectively; L_1 and L_2 are the length of the contraction and expansion segments of the micronozzle, respectively; R is the arc radius of the throat transition segment. The structural dimensions of the micronozzle are $L_{\rm in}=70\mu$m, $L_{\rm t}=30\mu$m, $L_{\rm out}=138\mu$m, $L_1=48\mu$m, $L_2=157\mu$m, $R=30\mu$m, $\theta_1=30^\circ$, $\theta_2=20^\circ$, and the etching depth of the nozzle is 300μm. The simulated gas medium is nitrogen, the inlet temperature is 300K, and the outlet pressure is 400Pa. The particle velocity space is discretized with 20×20 mesh points based on

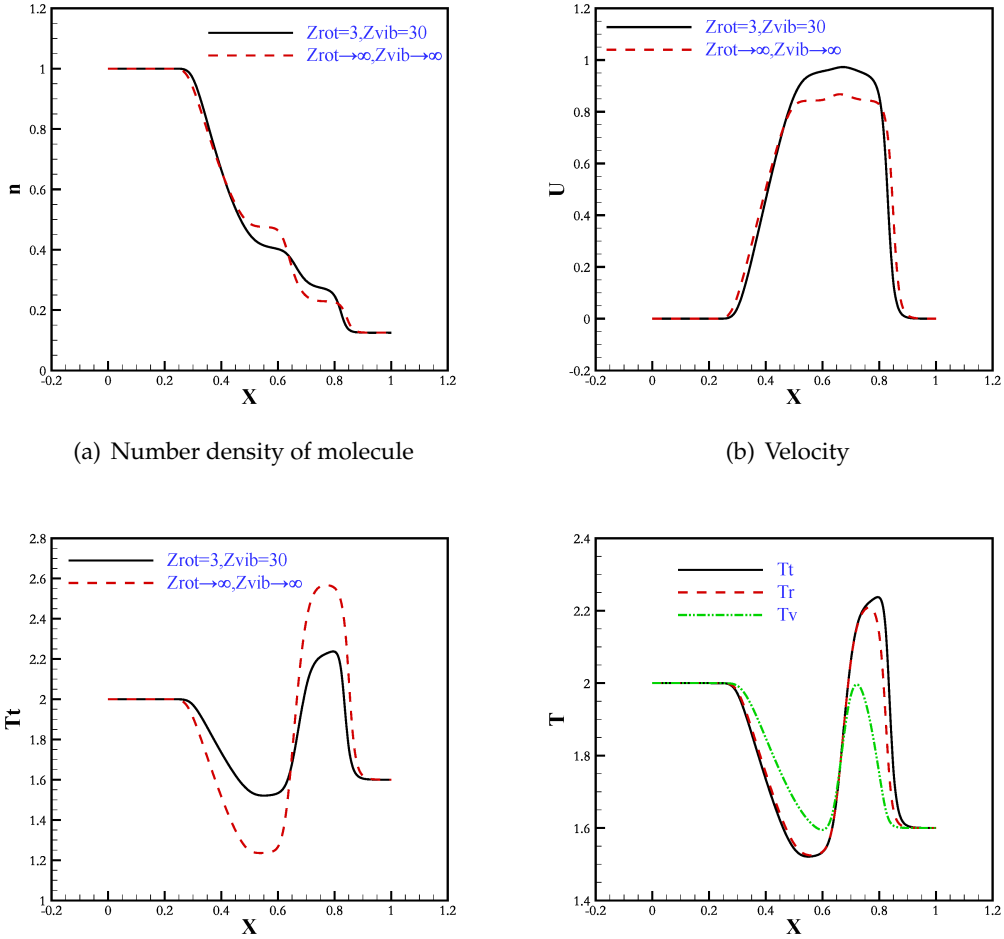

(a) Number density of molecule (b) Velocity

(c) Translational temperature (d) Temperature

Figure 2: Distribution of shock tube flow parameters $(Z_{\text{rot}}=3, Z_{\text{vib}}=30)$.

Gauss-Hermite rule. When the residual is less than 1E-6, the calculation is considered to be convergent.

Fig. 4 shows the comparison of nozzle outlet performance parameters under different inlet pressures. Thrust F_t and specific impulse I_{sp} are important parameters to characterize the propulsion performance of the nozzle, both are defined respectively: $F_t=\int_0^{L_{\text{out}}}\left(\rho_{out}u_{out}^2+p_{out}\right)b\mathrm{d}y$, $I_{sp}=F_t/\dot{m}g$, $\dot{m}=\int_0^{L_{\text{out}}}\rho_{out}u_{out}\mathrm{d}y$. Where ρ_{out}, u_{out} and p_{out} correspond to the density, velocity and pressure at the nozzle outlet, b is the etching depth, $\dot{m}$ is the mass flow rate at the outlet section, and g is the gravitational acceleration. Fig. 4(a) and (b) show the comparison between the thrust and specific impulse calculated

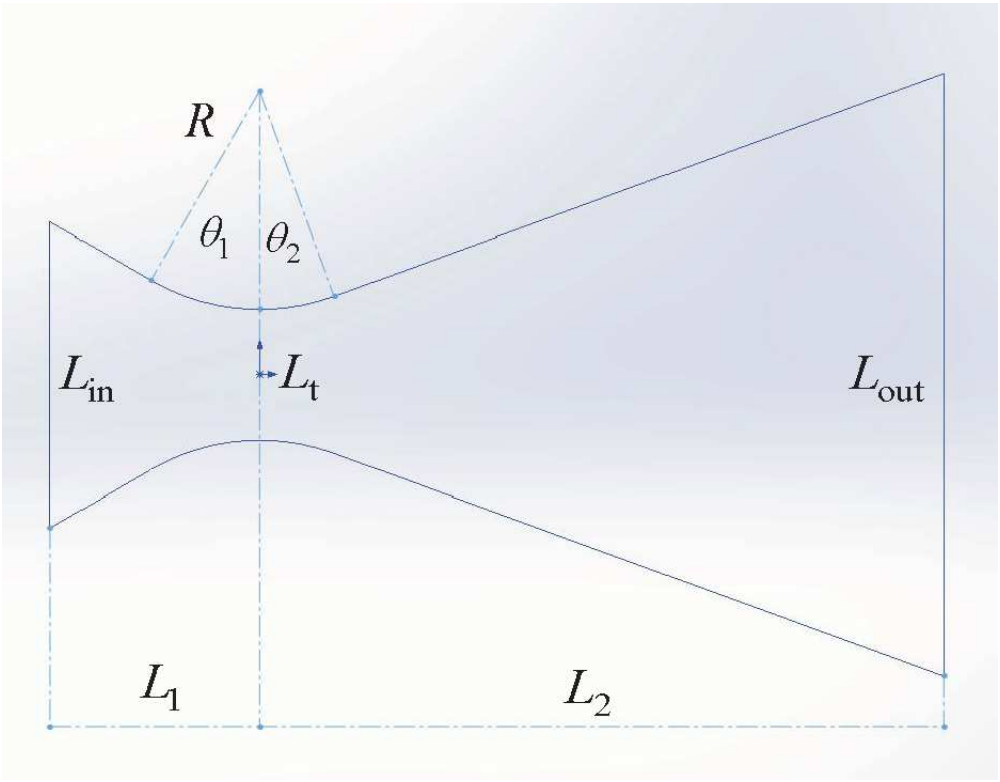

Figure 3: Micronozzle structure.

in this paper and those given in Ref. [29] under the four conditions of inlet pressure of 0.1atm, 0.5atm, 1.0atm and 2.0atm. It can be seen from the figure that the two are in good agreement, and the maximum relative error is 1.6%. As the inlet pressure increases, the thrust and mass flow rate increase accordingly. Since the mass flow rate is proportional to the outlet velocity, and the thrust is proportional to the square of the outlet velocity, the thrust growth rate is faster than the mass flow rate, so the specific impulse also increases accordingly. The variation trend of thrust and specific impulse in Fig. 4 and the variation trend of mass flow rate in Fig. 5 are consistent with the results of theoretical analysis.

Fig. 6 shows the contour distribution of rotational temperature, vibrational temperature and temperature distribution along the axis of the nozzle internal flow field at different inlet pressures. It can be seen from Fig. 6(a) that when the inlet pressure is 0.1atm, the translational temperature calculated in this paper is different from the DSMC calculation result given in reference [29]. The reasons are as follows: (1) the nozzle outlet condition calculated in this paper is an extrapolation, and the outlet boundary in reference is a pressure boundary; (2) In this paper, rotational energy excitation and vibrational energy excitation are considered. The simple gas model is used in the reference. In real gas flow, the vibrational energy will be partially converted into rotational energy and trans-

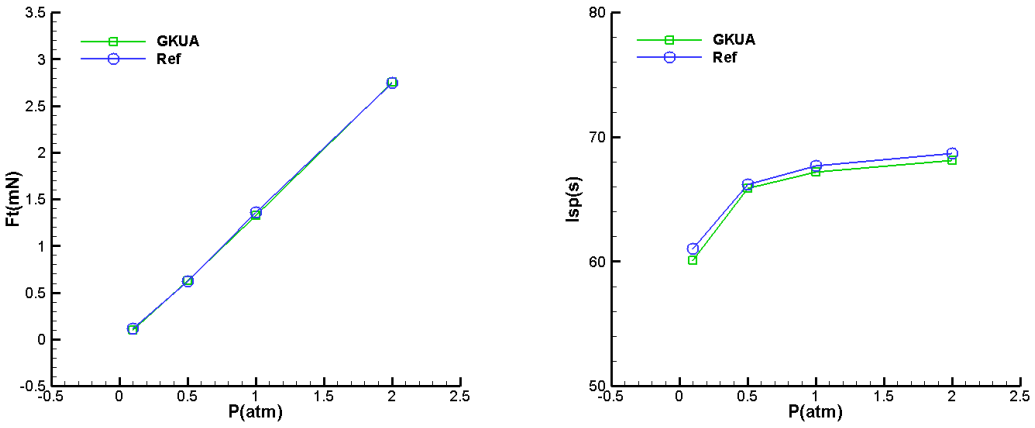

(a) Thrust (b) Specific impulse

Figure 4: Comparison of nozzle outlet performance parameters at different inlet pressures.

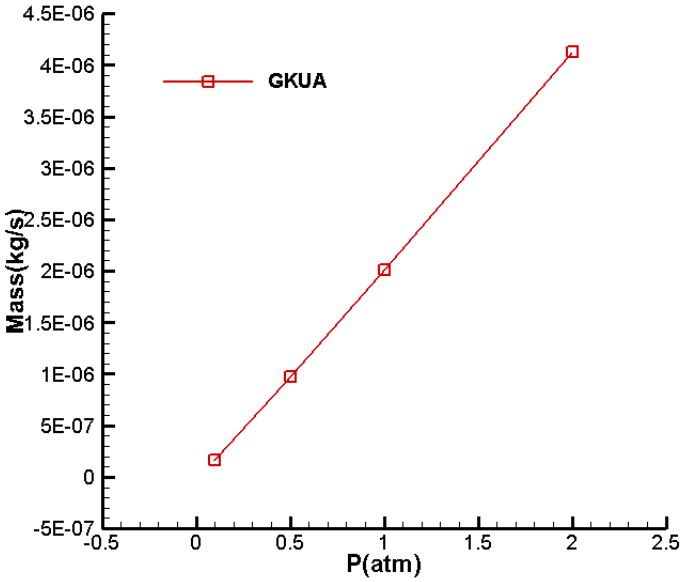

Figure 5: Mass flow rates at nozzle outlet calculated by the unified algorithm at different inlet pressures.

lational energy, so that the final translational temperature is higher than that obtained by the simple gas model, that is, the non-equilibrium effect of vibration will reduce the translational temperature at the outlet. As can be seen in Fig. 6(a), the vibrational and ro-

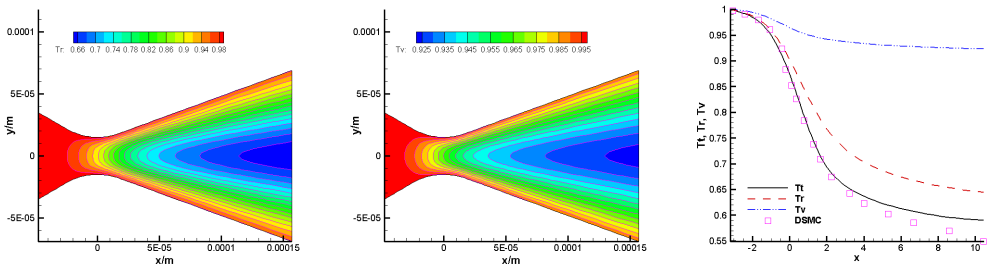

(a) 0.1atm inlet pressure

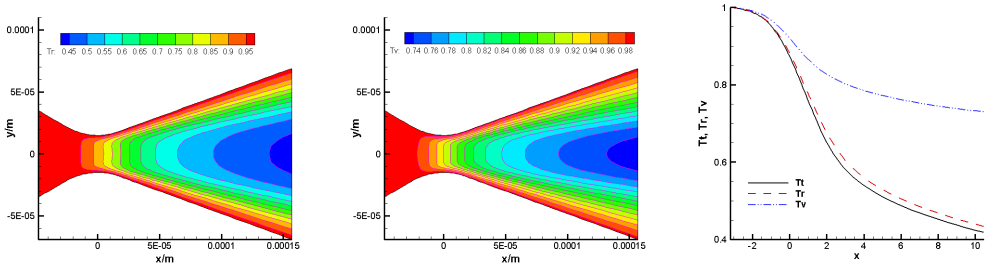

(b) 0.5atm inlet pressure

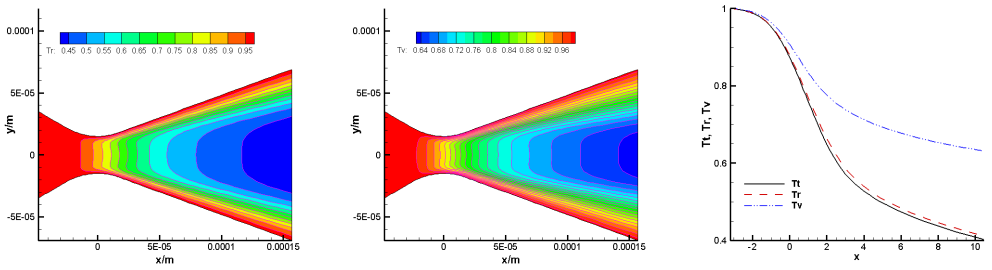

(c) 1.0atm inlet pressure

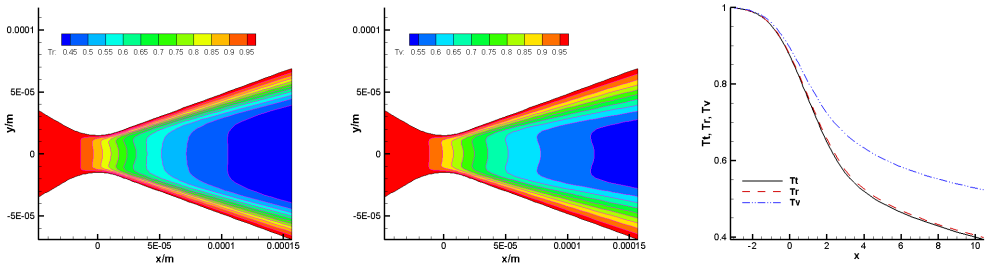

(d) 2.0atm inlet pressure

Figure 6: Temperature contour distribution and axis distribution of nozzle internal flow field under different inlet pressures.

tational energies are in non-equilibrium, especially the vibrational energy, which is close to the frozen state in the posterior part of the throat. Compared with Fig. 6(a)-(d), it can be seen that with the increase of inlet pressure, the non-equilibrium phenomenon of vibrational energy and rotational energy gradually becomes weaker. It can be seen that the increase of inlet pressure can indeed suppress the non-equilibrium effect of nozzle flow. The reason is that the collision frequency between particles is increased, so that the flow region in the nozzle is in the lower Knudsen number range, and the flow non-equilibrium phenomenon in the nozzle is delayed.

3.3 Analysis of two-dimensional nozzle internal and external mixed flow field of 25N attitude control engine

25N attitude control engine nozzle is shown in Fig. 7. Nozzle profile parameters are as follows: nozzle inlet diameter is 9.0mm, throat diameter is 2.77mm, outlet diameter is 8.82mm, contraction section length is 12.72mm, expansion section length is 8.26mm. The combustion chamber temperature is 3000K, the inlet Knudsen number is set to 0.0009, and the external environment is vacuum. The particle velocity space is discretized with 32×32 mesh points based on Gauss-Hermite rule. When the residual is less than 1E-6, the calculation is considered to be convergent.

The boundary of the internal and external mixed flow field of engine nozzle is shown in Fig. 8. For the vacuum boundary, the upper and right side boundaries are set as extrapolations, and the left side boundary is treated as follows: the velocity distribution function is taken to be zero when the molecule enters the flow field, and is extrapolated from internal flow field when the molecule leaves the flow field.

Fig. 9 shows the multi-block abutting grid of the internal and external mixed flow field of engine nozzle. The local encryption is carried out near the wall and the inner

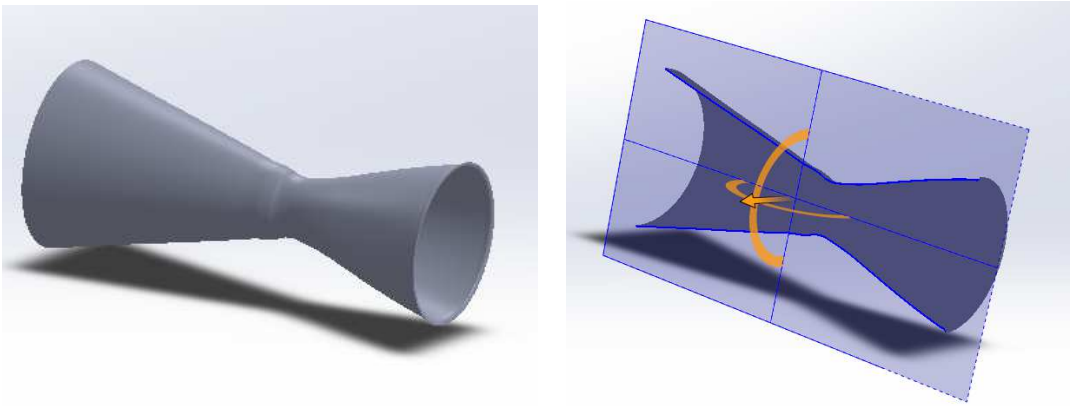

(a) Three-dimensional model (b) Profile

Figure 7: Schematic diagram of 25N attitude control engine nozzle.

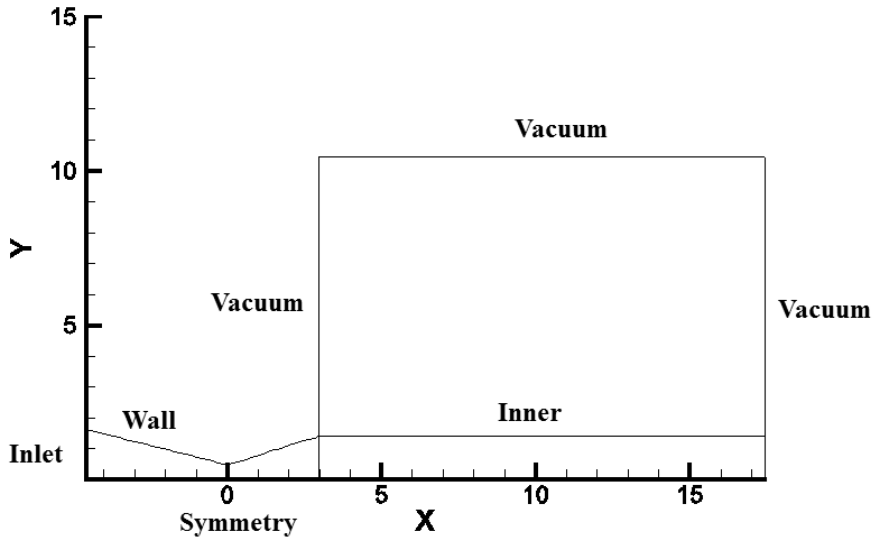

Figure 8: Schematic diagram of the boundaries of the internal and external mixed flow field.

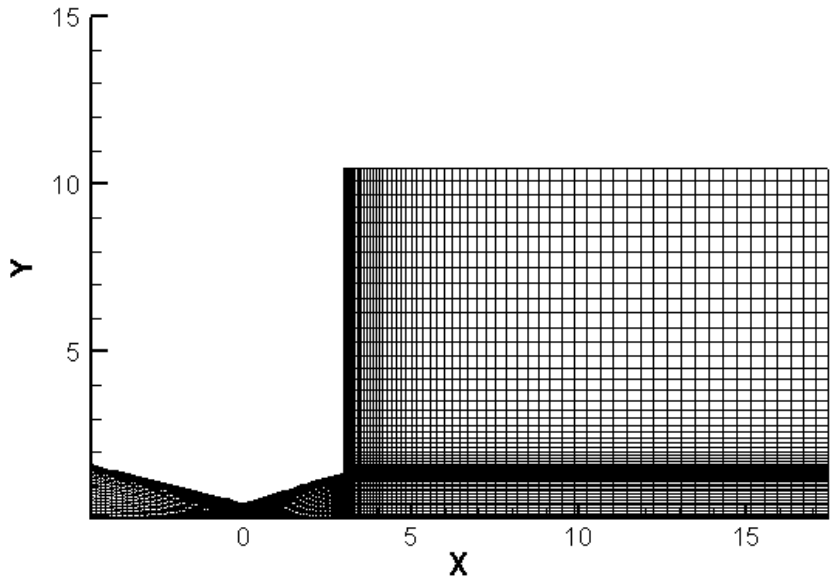

Figure 9: Schematic diagram of multi-block abutting grid of the internal and external mixed flow field.

boundary, and there are different grid changes among different multi-blocks according to the characteristics of flow field. Relatively, the inner field of the nozzle is dense, and the outer field is sparse.

3.3.1 Evolution law of internal and external mixed flow field at different times

Figs. 10-18 show the macroscopic flow parameter distribution (coordinate axis unit is m) of the internal and external mixed flow field considering vibrational energy excitation at nine different times, which are roughly divided into initial stage, development stage and stable stage. When $\widetilde{t}=0.0$ is the initial moment, the nozzle is filled with static gas, there is a pressure difference between the inlet and outlet, the temperature of the interior

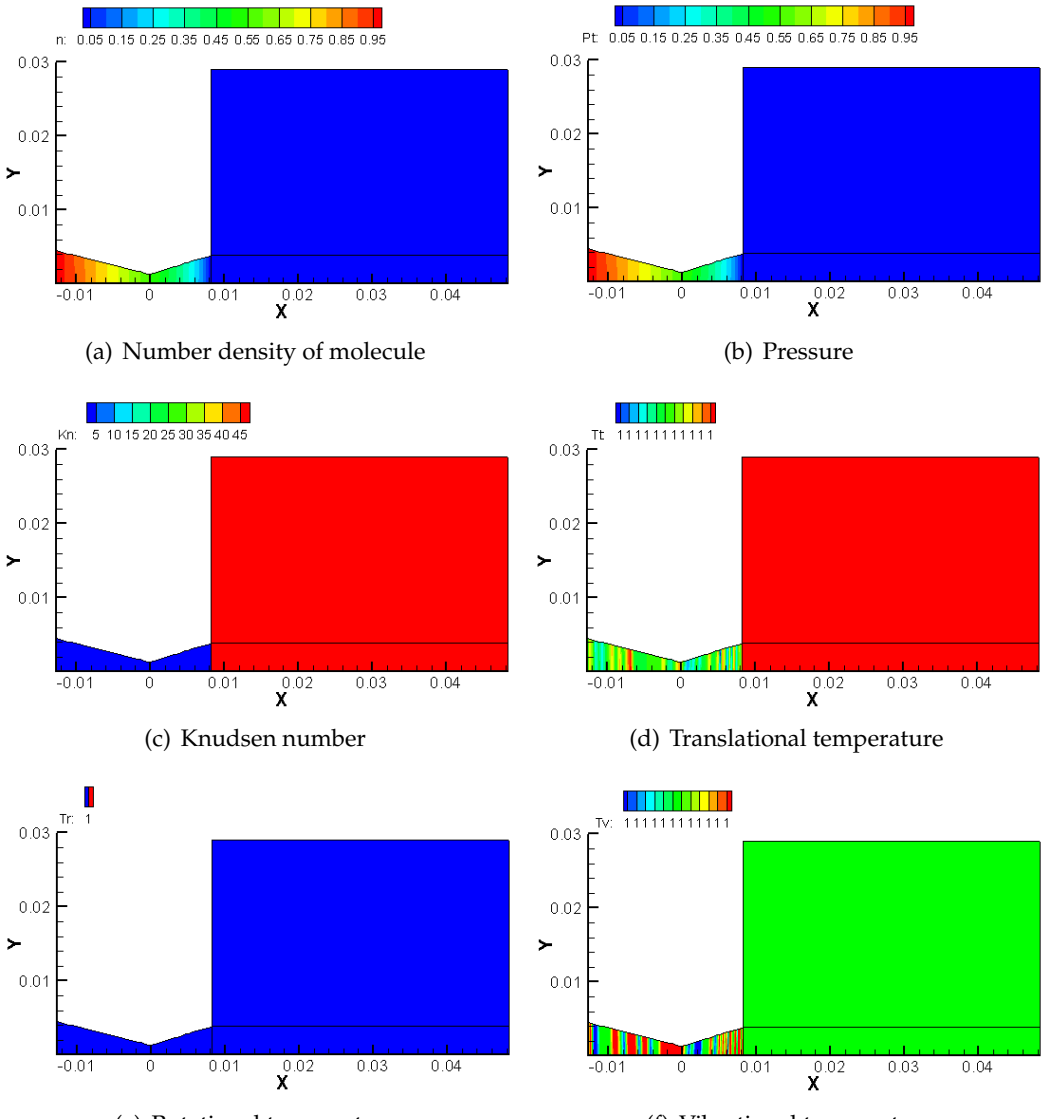

(a) Number density of molecule

(b) Pressure

(c) Knudsen number

(d) Translational temperature

(e) Rotational temperature

(f) Vibrational temperature

Figure 10: Distribution of macroscopic flow parameters in internal and external mixed flow field $(\widetilde{t}=0.0)$.

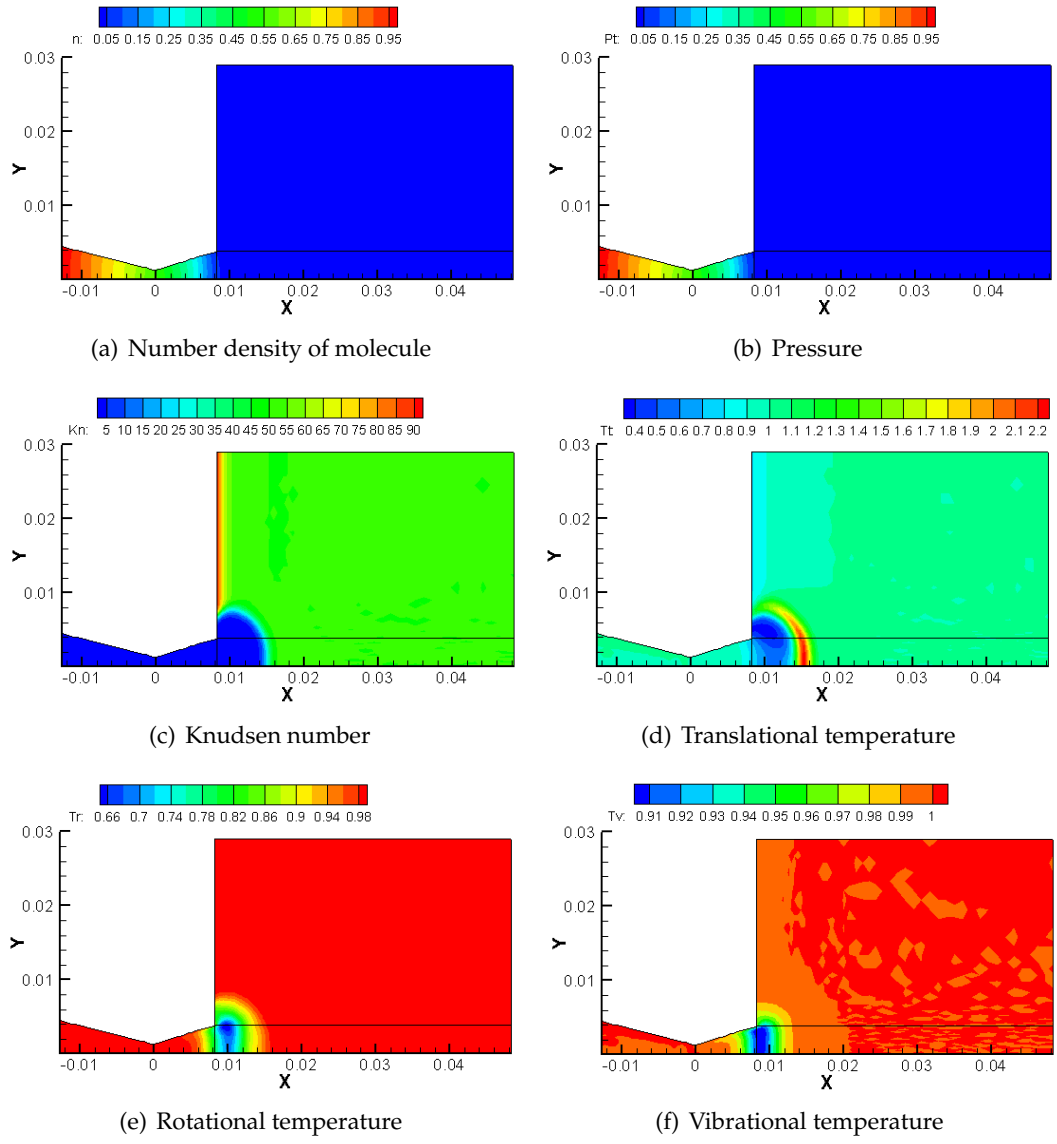

(a) Number density of molecule (b) Pressure

(c) Knudsen number (d) Translational temperature

(e) Rotational temperature (f) Vibrational temperature

Figure 11: Distribution of macroscopic flow parameters in internal and external mixed flow field $(\widetilde{t}=0.84)$.

and the external field is set to the same, the molecular number density of the external field is close to zero, the pressure is close to zero, and the Knudsen number is greater than 45. With the flow of time, the gas begins to enter the vacuum environment from the nozzle exit. For $\widetilde{t}=0.84$, the gas moves in vacuum for a short time. As can be seen from Fig. 11(a), the molecular number density contour extends partially to the vacuum external field, and the gas has entered the vacuum environment. As the gas enters, the gas Knudsen number near the nozzle exit begins to become smaller, and the area not

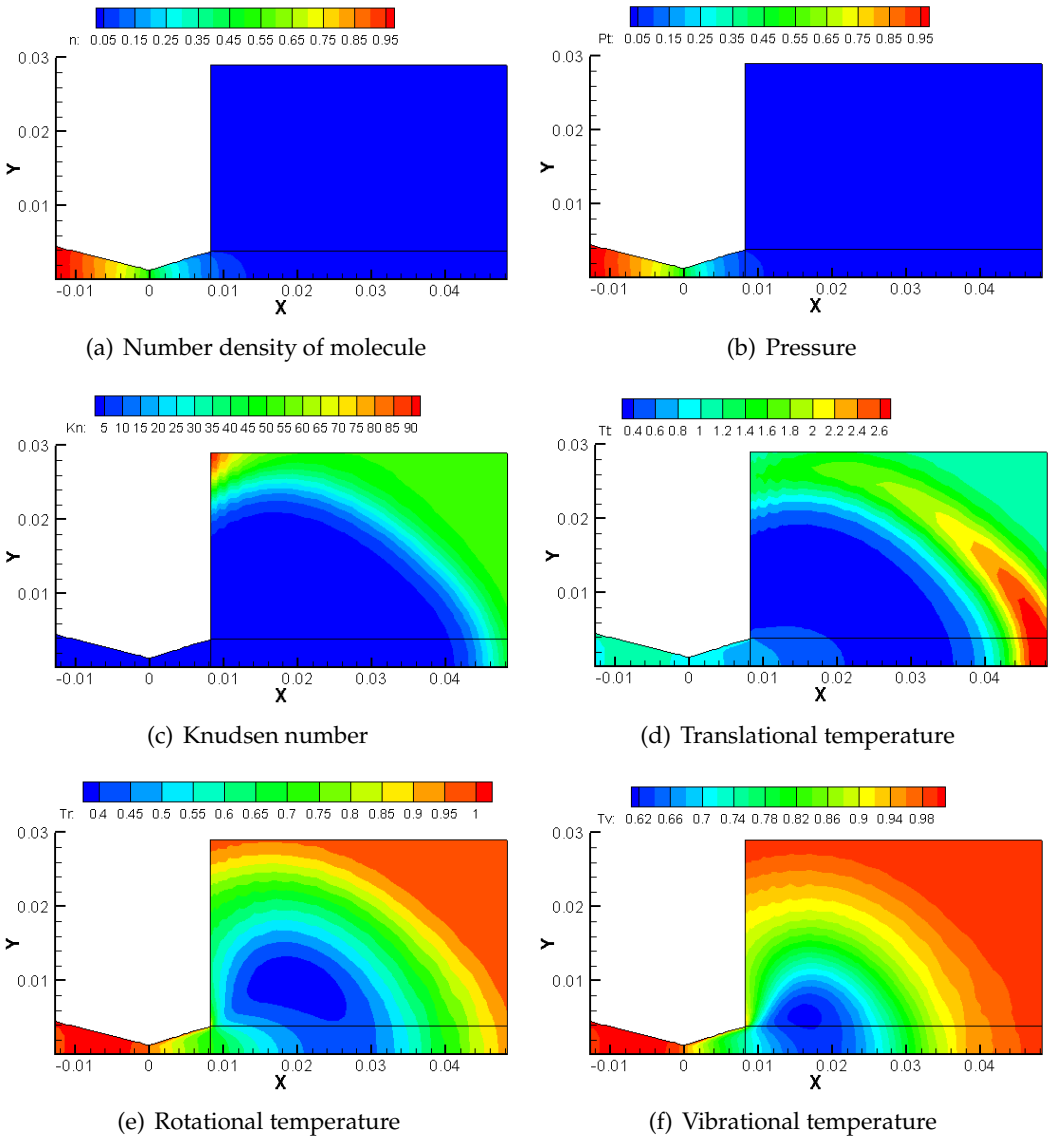

(a) Number density of molecule (b) Pressure

(c) Knudsen number (d) Translational temperature

(e) Rotational temperature (f) Vibrational temperature

Figure 12: Distribution of macroscopic flow parameters in internal and external mixed flow field $(\widetilde{t}=4.2)$.

reached by the external field is still a high Knudsen number. The Knudsen number at the left vacuum boundary is greater than 90, which is due to the influence of boundary assignment. However, it does not affect the calculation of the infield region. From the observation of the translational temperature in Fig. 11(d), it can be seen that there is a high temperature zone in the front section of the gas during the movement of the gas. The reason is that the vacuum environment of the calculation example is not strictly vac-

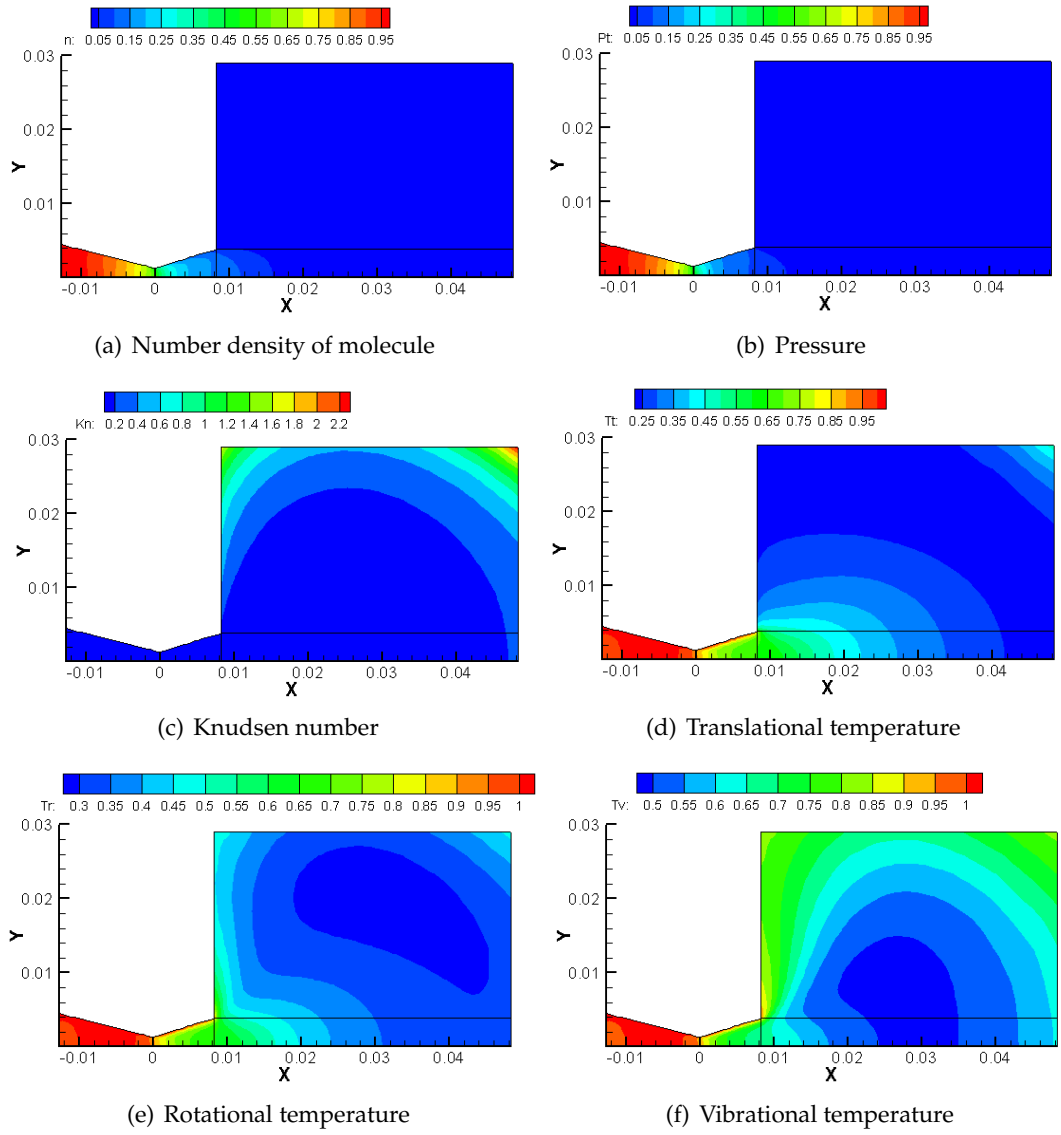

(a) Number density of molecule (b) Pressure

(c) Knudsen number (d) Translational temperature

(e) Rotational temperature (f) Vibrational temperature

Figure 13: Distribution of macroscopic flow parameters in internal and external mixed flow field $(\widetilde{t}=8.4)$.

uum. In order to be able to perform the calculation simulation, the vacuum region is set to be close to vacuum, and there are still a few gas molecules, and the incoming gas molecules collide with the remaining stationary gas molecules, resulting in energy conversion. When $\widetilde{t}=8.4$, the gas molecules entering first are about to leave the axial calculation region, and the dense region of the external field becomes larger, and the molecular number density increases. When $\widetilde{t}=12.6$, the gas molecules entering first have left the calculation region. In the whole calculation region, the gas molecular number density is

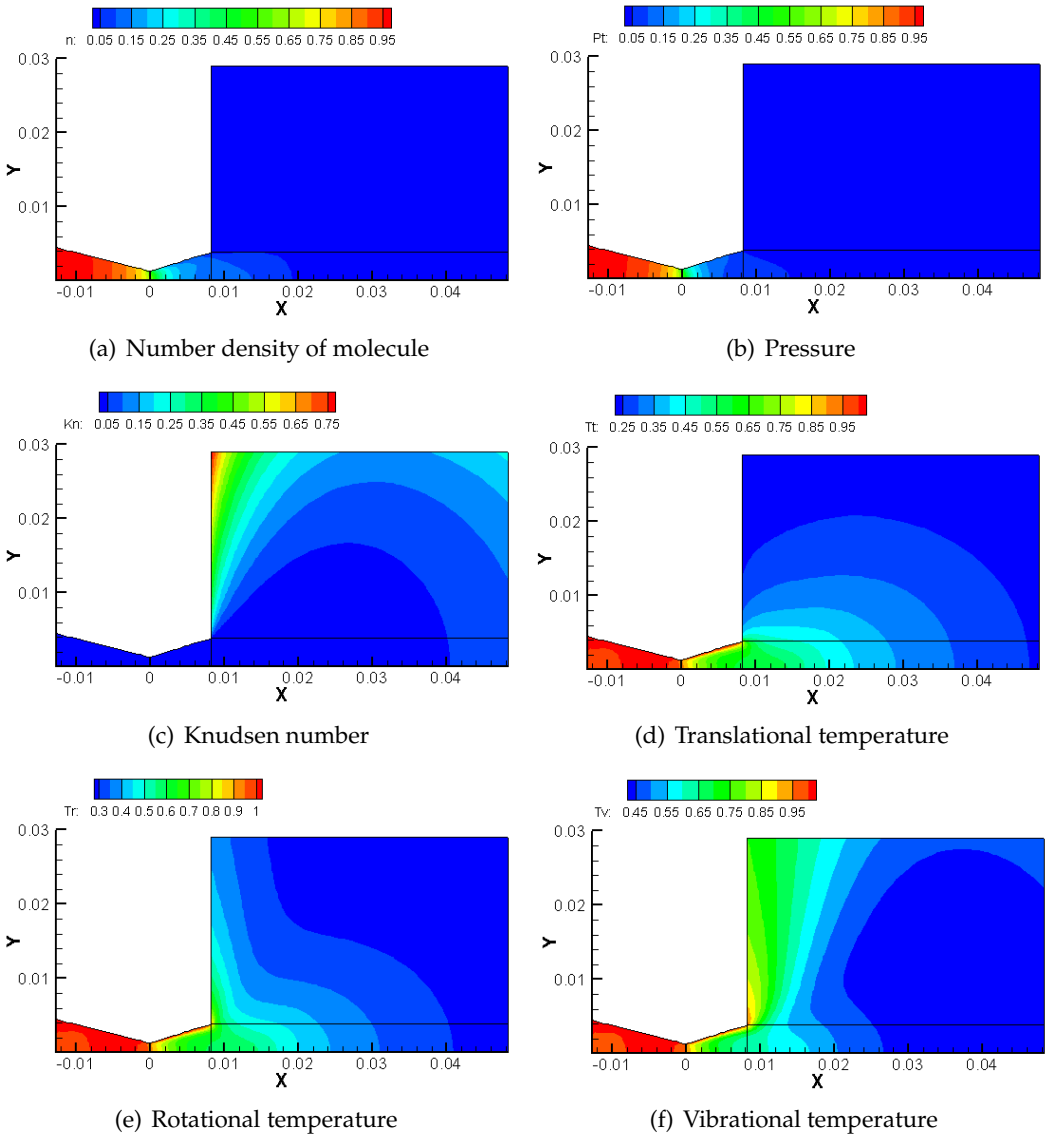

(a) Number density of molecule (b) Pressure

(c) Knudsen number (d) Translational temperature

(e) Rotational temperature (f) Vibrational temperature

Figure 14: Distribution of macroscopic flow parameters in internal and external mixed flow field $(\widetilde{t}=12.6)$.

distributed near the nozzle outlet axis, and the molecular number density away from the axis is lower. According to Fig. 14(c), the distribution area of gas molecules presents a circular calabash expansion, indicating that gas molecules mainly move along the axial direction and less radial direction. When $\widetilde{t}=33.6$, the flow field in the calculated area has begun to approach stability, and when $\widetilde{t}=55$, the flow field reaches the set convergence condition. At this time, the Knudson number in the calculated area gradually increases along the nozzle outlet lip upward, and the rarefaction degree is obvious. The external

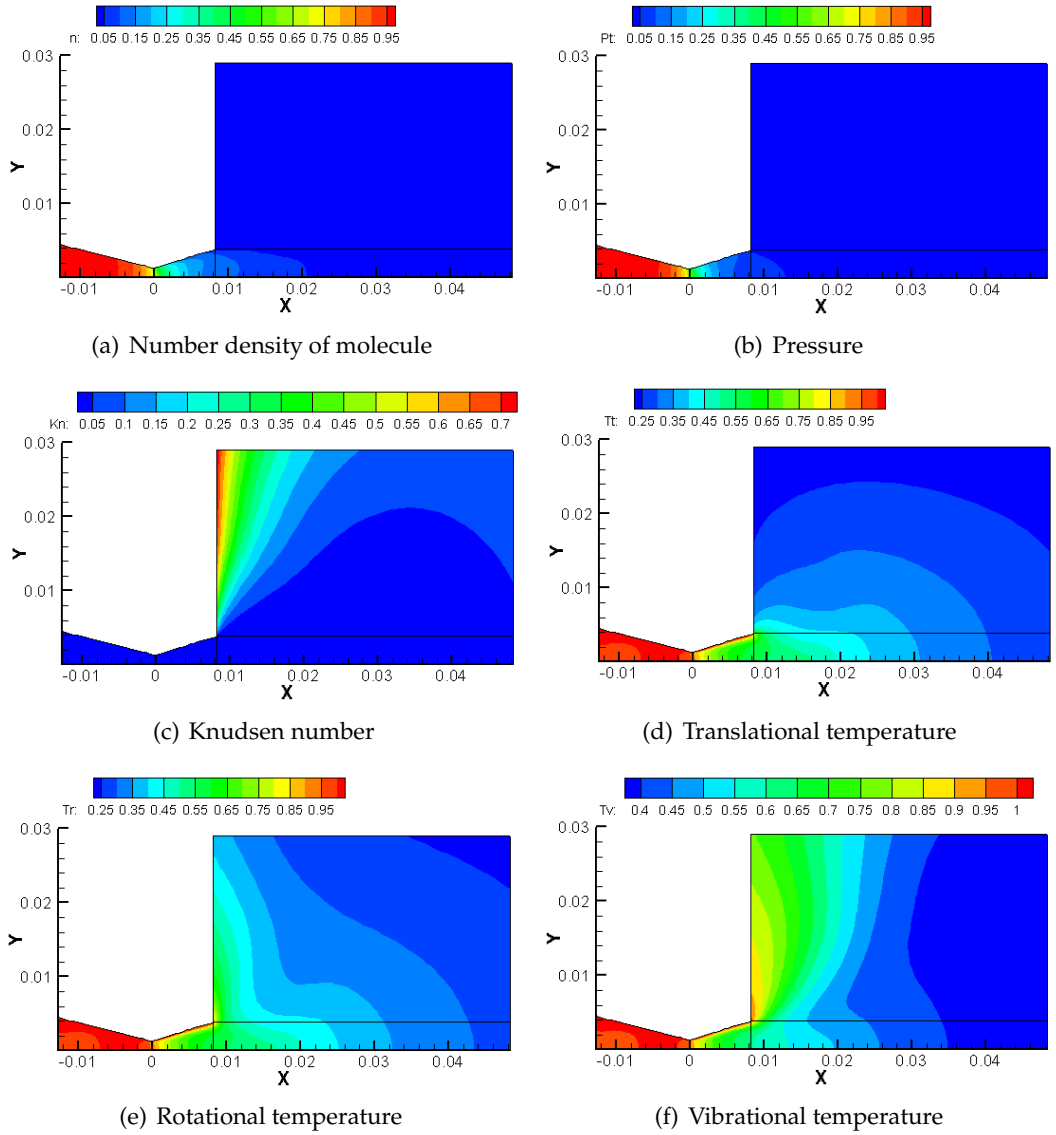

(a) Number density of molecule

(b) Pressure

(c) Knudsen number

(d) Translational temperature

(e) Rotational temperature

(f) Vibrational temperature

Figure 15: Distribution of macroscopic flow parameters in internal and external mixed flow field $(\tilde{t}=16.8)$.

field translational temperature is distributed as a circular arc from the nozzle outlet, the rotational temperature is distributed as a single peak, and the vibrational temperature is distributed as a double peak, which looks like "W". From the perspective of the distribution of translational, rotational and vibrational temperature, the vibrational temperature at the nozzle outlet and the backward area is the highest, followed by rotational temperature and translational temperature. This also means that there is a strong internal energy non-equilibrium effect after the high-temperature gas enters the vacuum from the nozzle.

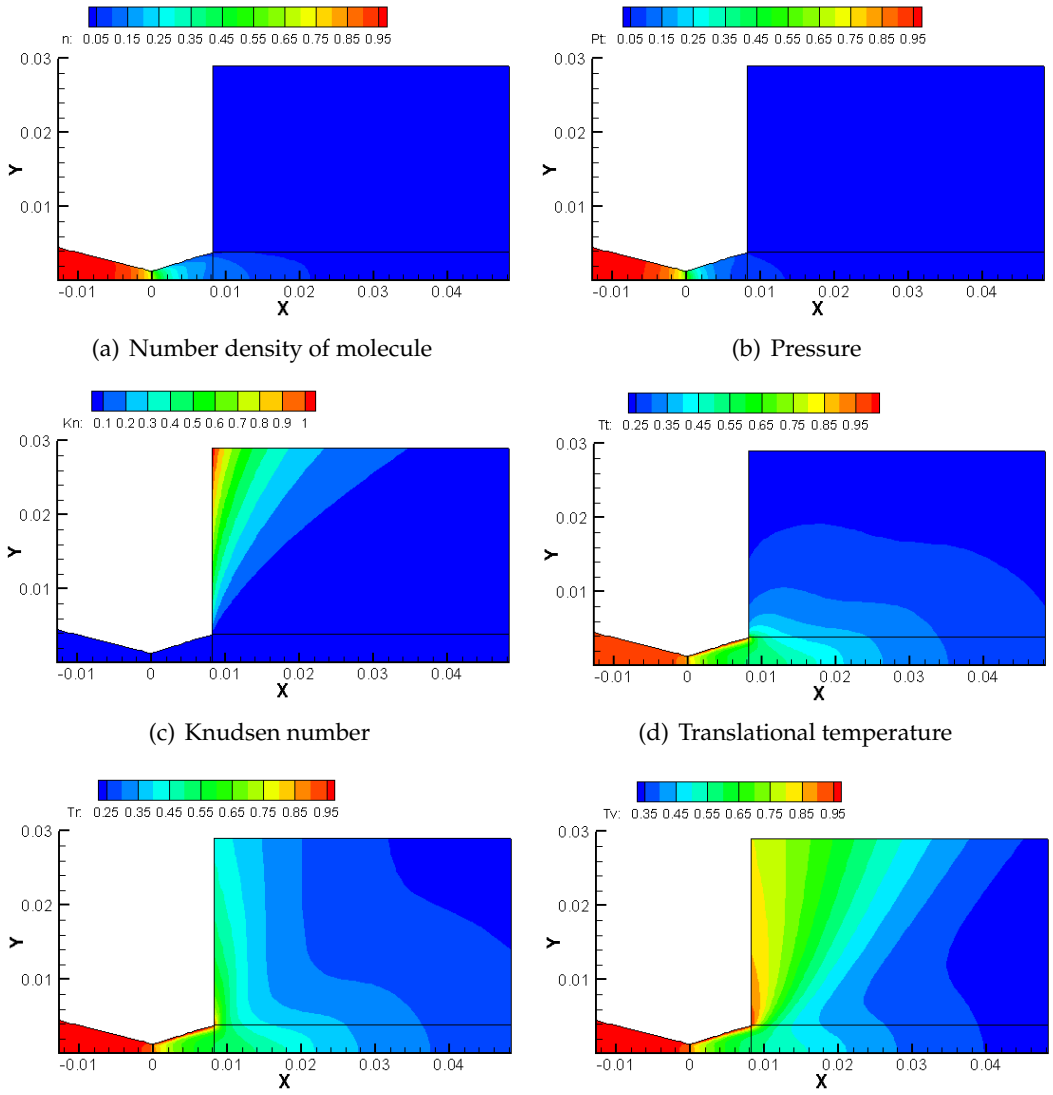

(a) Number density of molecule (b) Pressure

(c) Knudsen number (d) Translational temperature

(e) Rotational temperature (f) Vibrational temperature

Figure 16: Distribution of macroscopic flow parameters in internal and external mixed flow field $(\widetilde{t}=33.6)$.

Fig. 19 shows the Mach number distribution and streamline distribution of the mixed flow field at eight different times. The red solid line marked in the figure is the regional range of gas diffusion at different times. It can be seen from the figure that the gas diffuses in a feather-like manner in the vacuum environment. As time goes by, the feather-like diffusion range becomes larger and larger, until it exceeds the calculation area. As can be seen from Fig. 19(h), when the flow field is stable, the area above the nozzle lip streamlines backward, and part of the gas flows out from the left side of the area above,

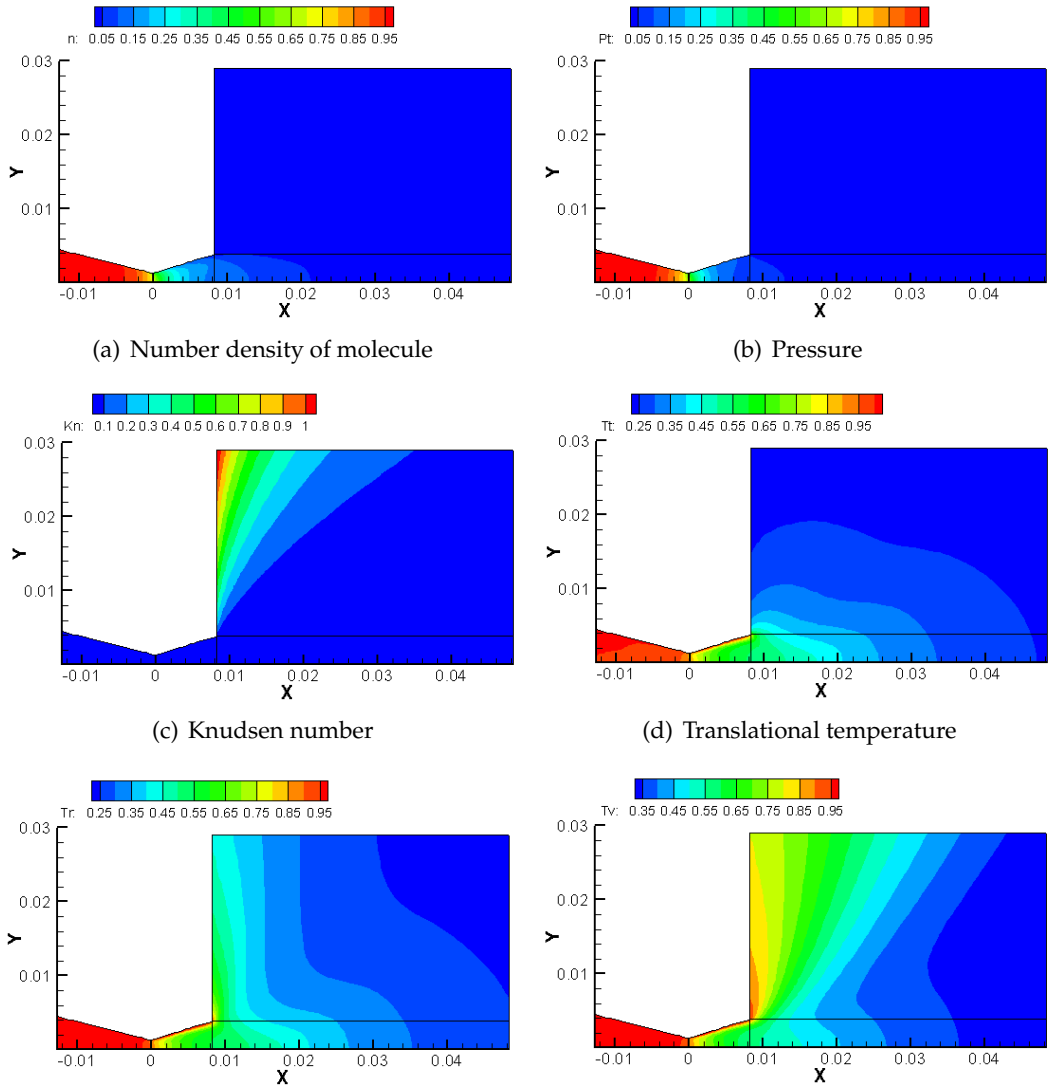

(a) Number density of molecule (b) Pressure

(c) Knudsen number (d) Translational temperature

(e) Rotational temperature (f) Vibrational temperature

Figure 17: Distribution of macroscopic flow parameters in internal and external mixed flow field $(\widetilde{t}=50.39)$.

forming gas backflow. Fig. 20 shows the velocity contour distribution of the steady flow field, where the blue part is the region where the axial velocity is less than zero, which is the backflow region. The backflow region starts from the nozzle outlet lip and gradually increases the range with the radial direction.

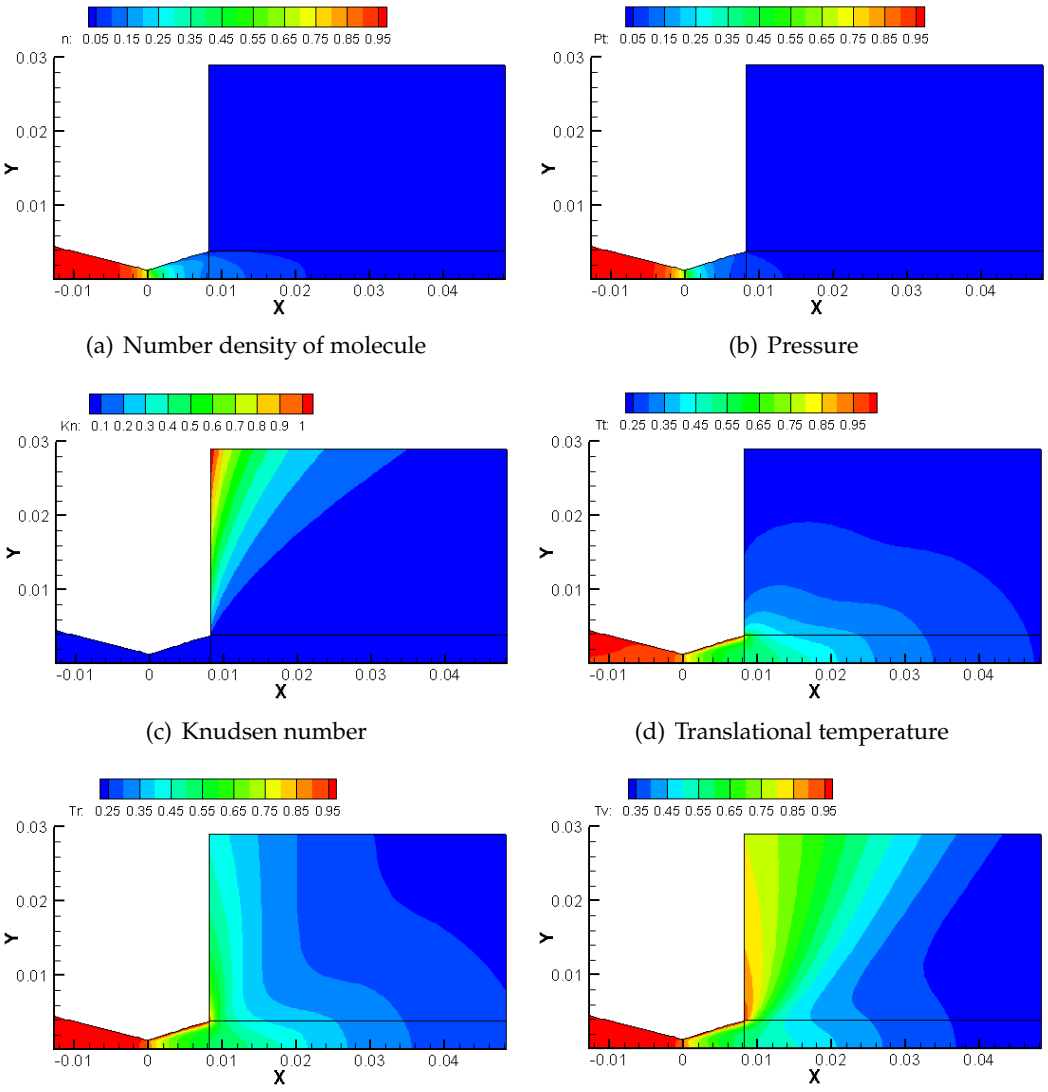

(a) Number density of molecule (b) Pressure

(c) Knudsen number (d) Translational temperature

(e) Rotational temperature (f) Vibrational temperature

Figure 18: Distribution of macroscopic flow parameters in internal and external mixed flow field $(\widetilde{t}=55)$.

3.3.2 Evolution of molecular velocity distribution function at different positions on the axis

Fig. 21 shows the distribution of the rotational energy reduction velocity distribution function at $\widetilde{t}=0.0$ on the axis at different times. The area at $\widetilde{t}=0.0$ is the throat. It can be seen from the figure that at different times, the rotational energy reduction velocity distribution function at the throat presents a typical quasi-Gaussian distribution from the

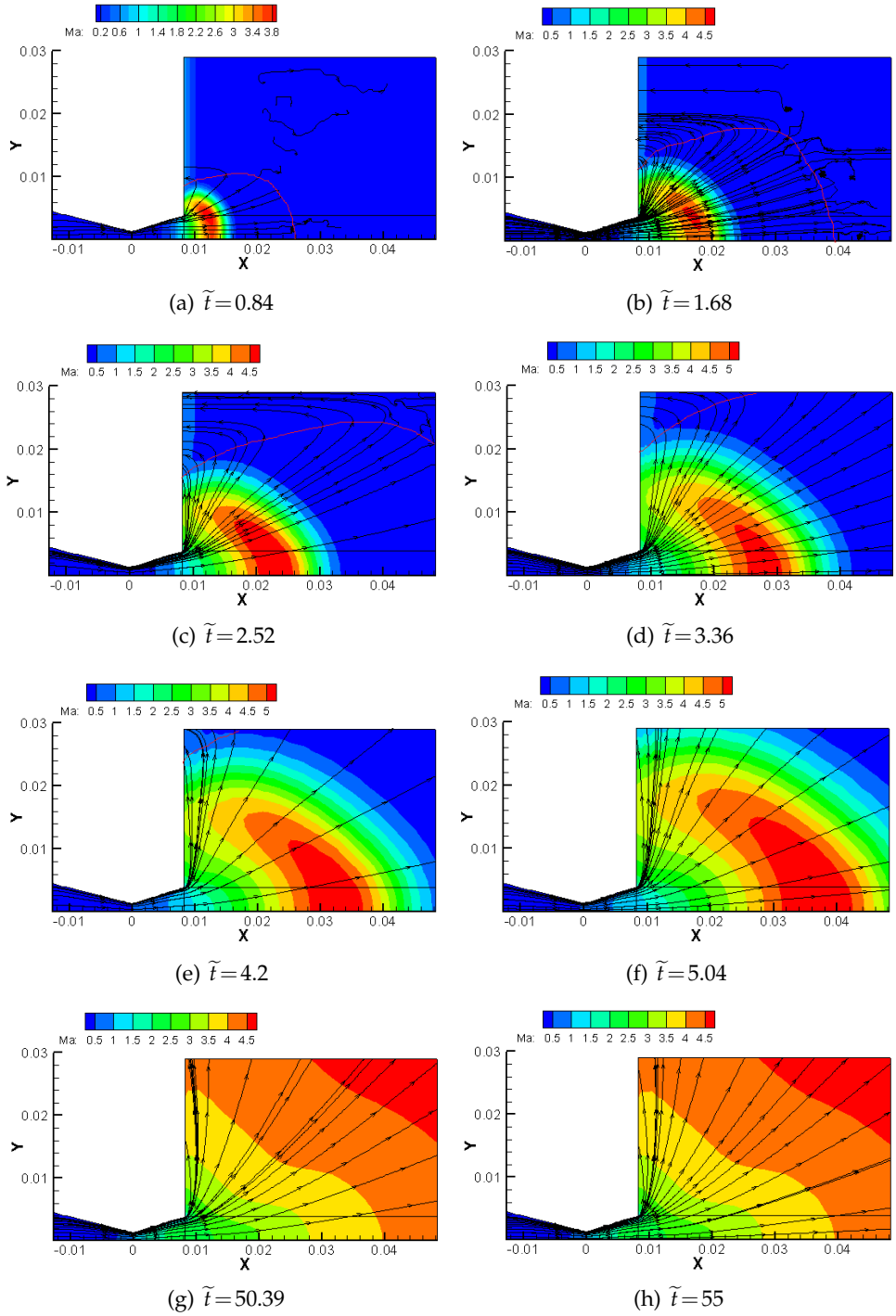

(a) $\widetilde{t}=0.84$ (b) $\widetilde{t}=1.68$

(c) $\widetilde{t}=2.52$ (d) $\widetilde{t}=3.36$

(e) $\widetilde{t}=4.2$ (f) $\widetilde{t}=5.04$

(g) $\widetilde{t}=50.39$ (h) $\widetilde{t}=55$

Figure 19: Mach number distribution and streamline of flow field at different times.

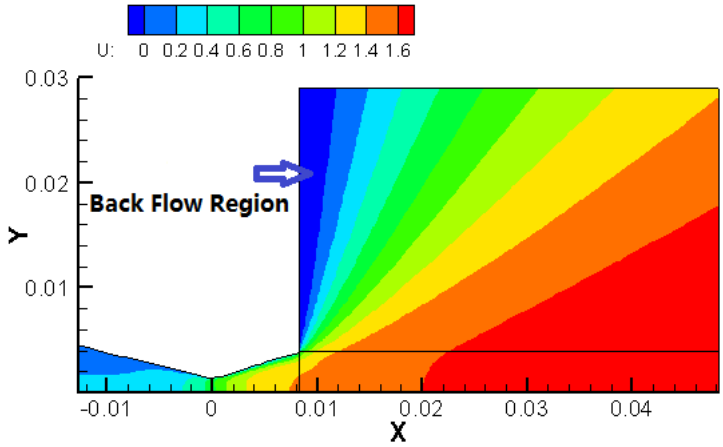

Figure 20: Schematic diagram of the backflow region.

initial stage, the development stage to the stable stage. Since it is on the axis and the radial velocity is zero, the distribution center is always on the line $V_y = 0$, and the distribution function is symmetric about the X direction. As the flow progresses, the axial velocity at the throat increases until it becomes stable, so the center of the distribution function shifts to the positive direction V_x with time. As the flow progresses, the temperature at the throat will gradually decrease until it is stable, so the distribution function will gradually become steeper until it is stable.

Fig. 22 shows the distribution of the vibrational energy reduction velocity distribution function at $\widetilde{x} = 0.0$ on the axis at different times. As can be seen from the figure, the reduced velocity distribution function of vibrational energy at the throat at different times from the initial stage, development stage to the stable stage presents a typical quasi-Gaussian distribution, which indicates that the vibrational energy at the center of the throat is always in a balanced state during the whole flow process of this example.

Fig. 23 shows the distribution of the rotational energy reduction velocity distribution function at $\widetilde{x} = 6.4213$ on the axis at different times. The area at $\widetilde{x} = 6.4213$ is the core area of the plume. It can be seen from the figure that at different times, the rotational energy reduction velocity distribution function of the core area of the plume from the initial stage, the development stage to the stable stage shows a typical quasi-Gaussian distribution, but there is a phenomenon that the irregular part of the image center becomes larger. This indicates that the rotational energy in the core region of the plume deviates from the equilibrium state to a small extent during the whole flow process in this example. From $\widetilde{t} = 1.68$ to $\widetilde{t} = 8.4$, the center of the distribution function shifts to the left, indicating that the axial velocity at $\widetilde{t} = 1.68$ is greater than that at $\widetilde{t} = 8.4$.

Fig. 24 shows the distribution of the vibrational energy reduction velocity distribution function at $\widetilde{x} = 6.4213$ on the axis at different times. It can be seen from the figure that at different times, the vibrational energy reduction velocity distribution function in the core

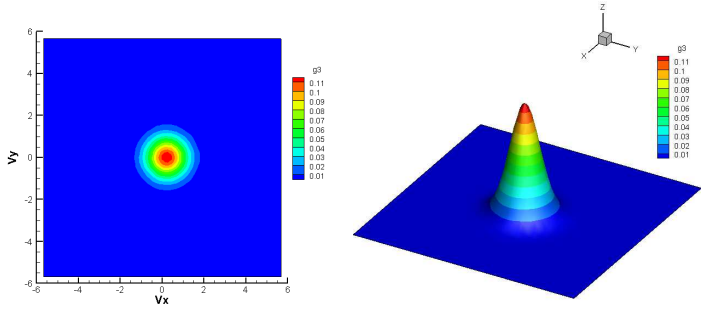

(a) $\widetilde{t}=1.68$

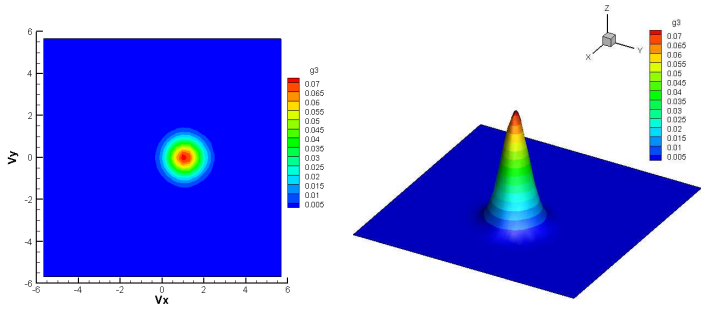

(b) $\widetilde{t}=8.4$

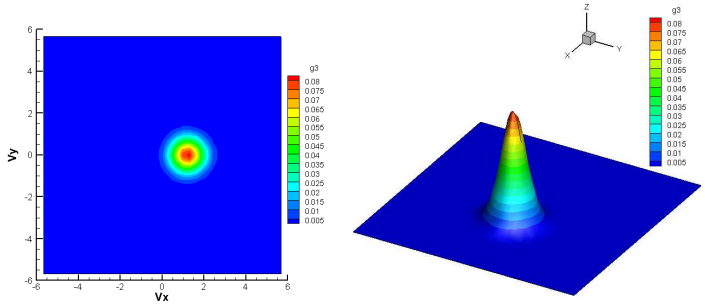

(c) $\widetilde{t}=33.6$

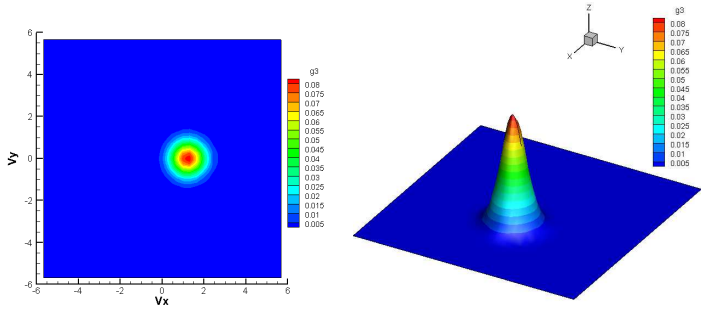

(d) $\widetilde{t}=53.75$

Figure 21: The rotational energy reduction velocity distribution function at $\widetilde{x}=0.0$ on the axis at different times.

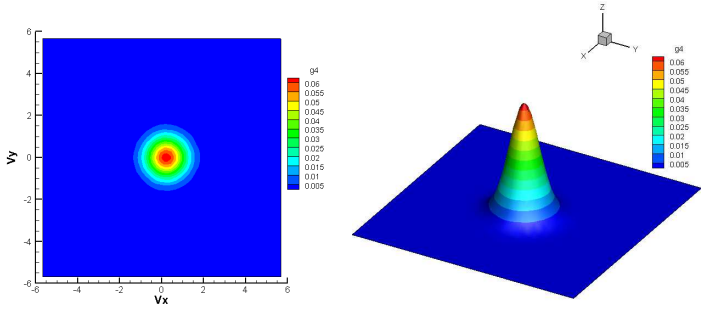

(a) $\widetilde{t}=1.68$

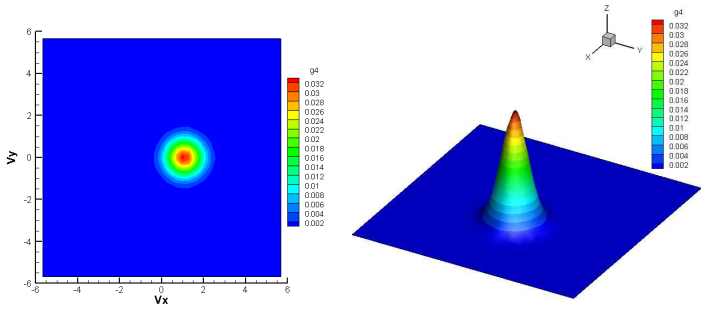

(b) $\widetilde{t}=8.4$

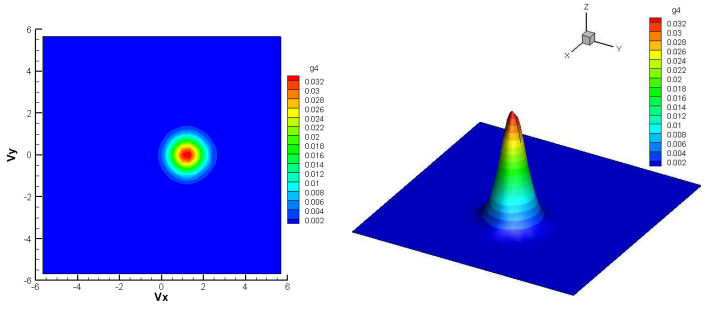

(c) $\widetilde{t}=33.6$

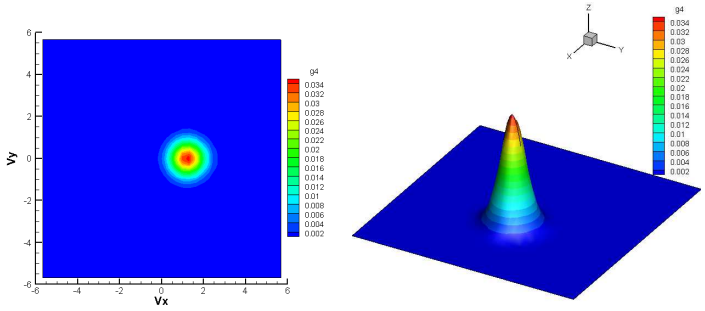

(d) $\widetilde{t}=53.75$

Figure 22: The vibrational energy reduction velocity distribution function at $\widetilde{x}=0.0$ on the axis at different times.

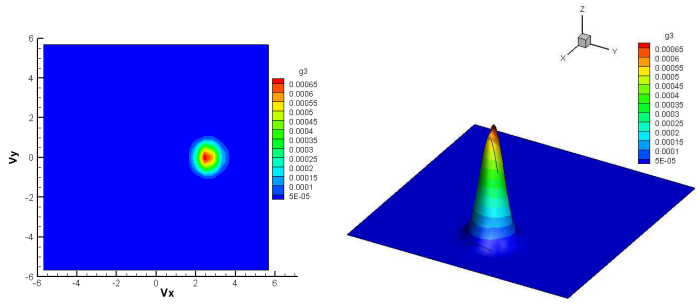

(a) $\widetilde{t}=1.68$

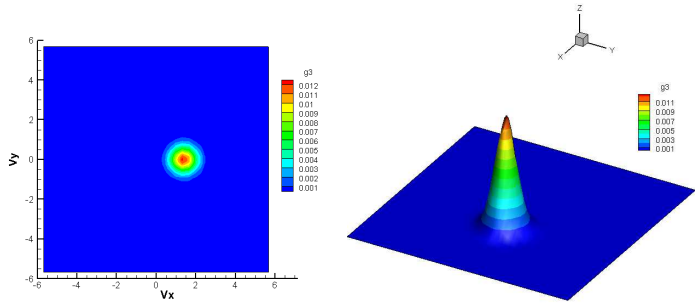

(b) $\widetilde{t}=8.4$

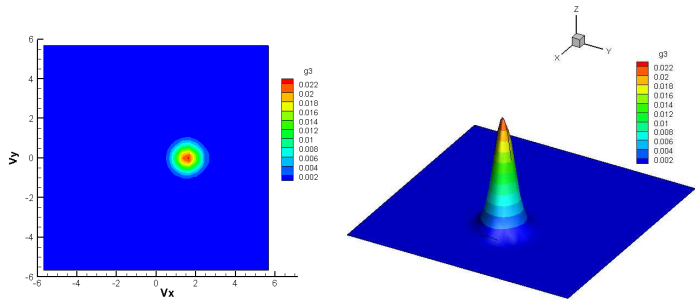

(c) $\widetilde{t}=33.6$

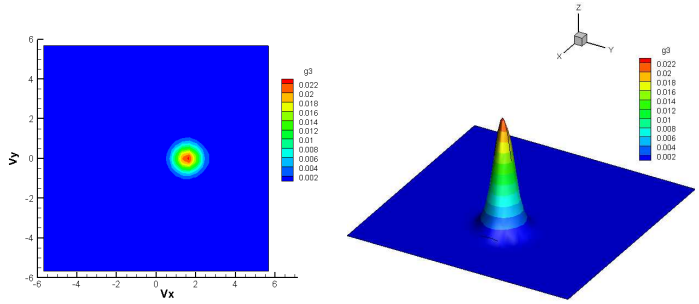

(d) $\widetilde{t}=53.75$

Figure 23: The rotational energy reduction velocity distribution function at $\widetilde{x}=6.4213$ on the axis at different times.

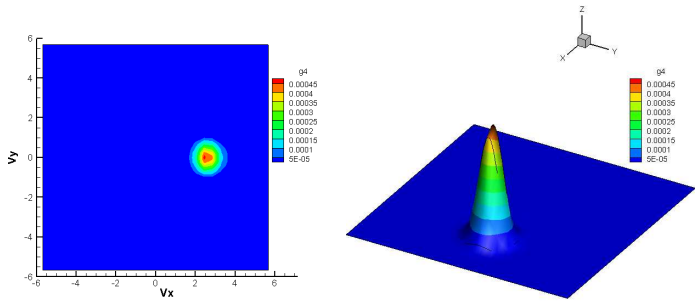

(a) $\widetilde{t}=1.68$

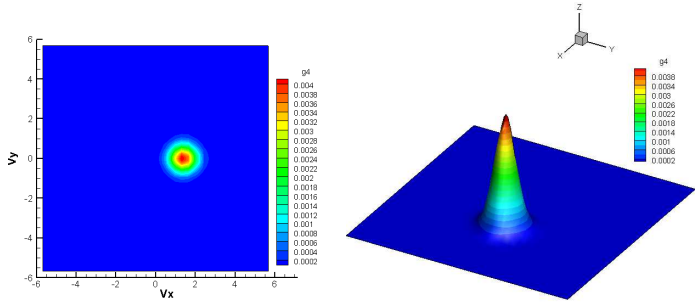

(b) $\widetilde{t}=8.4$

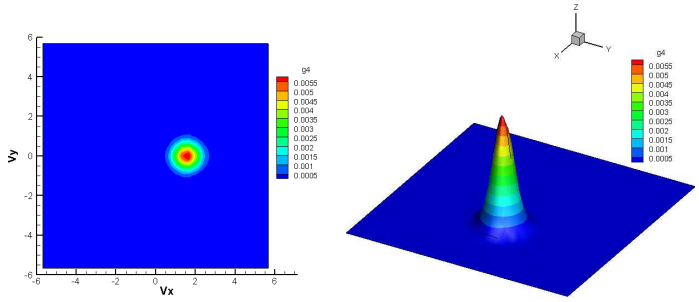

(c) $\widetilde{t}=33.6$

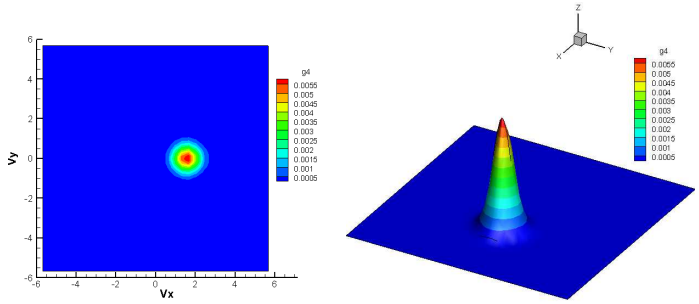

(d) $\widetilde{t}=53.75$

Figure 24: The vibrational energy reduction velocity distribution function at $\widetilde{x}=6.4213$ on the axis at different times.

region of the plume presents a typical quasi-Gaussian distribution from the initial stage, the development stage to the stable stage, but there is a phenomenon that the irregular part in the center of the image becomes larger and the outer region is irregular, which indicates that the vibrational energy in the core region of the plume deviates from the equilibrium state to a large extent during the whole flow process in this example.

3.3.3 Comparison among simple gas model, rotational energy model and vibrational energy model

Fig. 25 shows the distribution of the macroscopic temperature along the axis of the internal and external mixed flow field in the steady state. It can be seen from the figure that in the temperature distributions of the internal and external mixed flow field along the axis, the vibrational temperature is the highest, the rotational temperature is the second, and the translational temperature is the lowest, which confirms the temperature distribution phenomenon observed in Section 3.3.1. The rotational temperature distribution curve is very close to the translational temperature curve, indicating that the rotational energy is basically in equilibrium. The vibrational temperature curve begins to deviate from the rotational temperature curve in the expansion section of the nozzle. The reason is that the temperature of the expansion section drops sharply, the specific heat of gas cannot keep up with the change of temperature, and the vibrational energy is too late to converted into rotational energy and translational energy and then into kinetic energy, so energy loss will be caused.

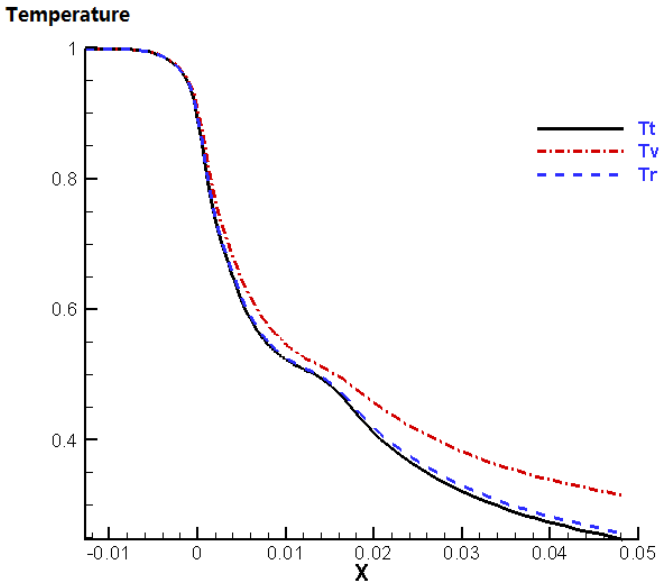

Figure 25: Macroscopic temperature distributions along the axis of the internal and external mixed flow field in a stable state.

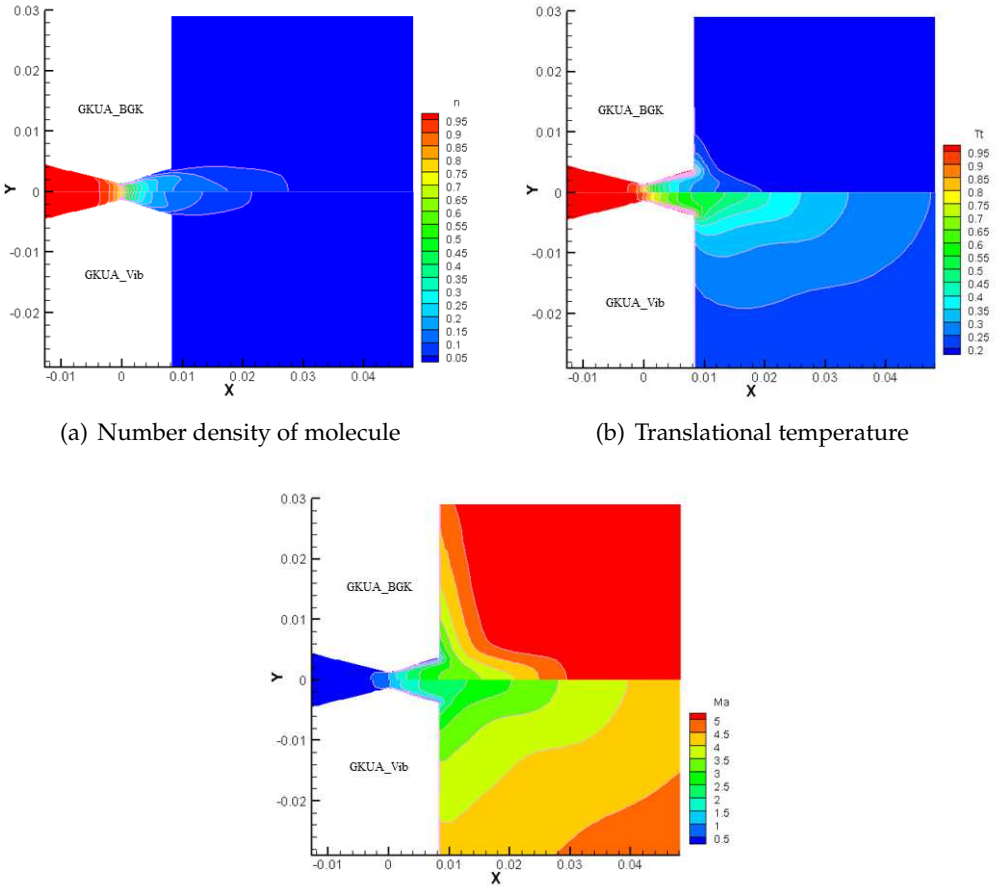

(a) Number density of molecule

(b) Translational temperature

(c) Mach number

Figure 26: Comparison of GKUA results between Boltzmann model equation with vibrational energy excitation and simple gas BGK model.

Fig. 26 shows a comparison between the calculation results of GKUA based on a simple gas BGK model (represented by "GKUA_BGK" in the figure) and the calculation results of the Boltzmann model equation unified algorithm considering vibrational energy excitation in this paper (represented by "GKUA_Vib" in the figure). The simple gas model only considers translational energy, which considers rotational and vibrational energy to be frozen, while the vibrational energy model considers internal energy excitation. In the process of the internal and external mixed flow of engine, the temperature and pressure decrease, the velocity increases, and the internal energy of gas molecules is converted into kinetic energy. When the internal energy excitation is considered, the vibrational energy and rotational energy will be converted into translational energy and kinetic energy. Compared with the simple gas model, the translational temperature will increase,

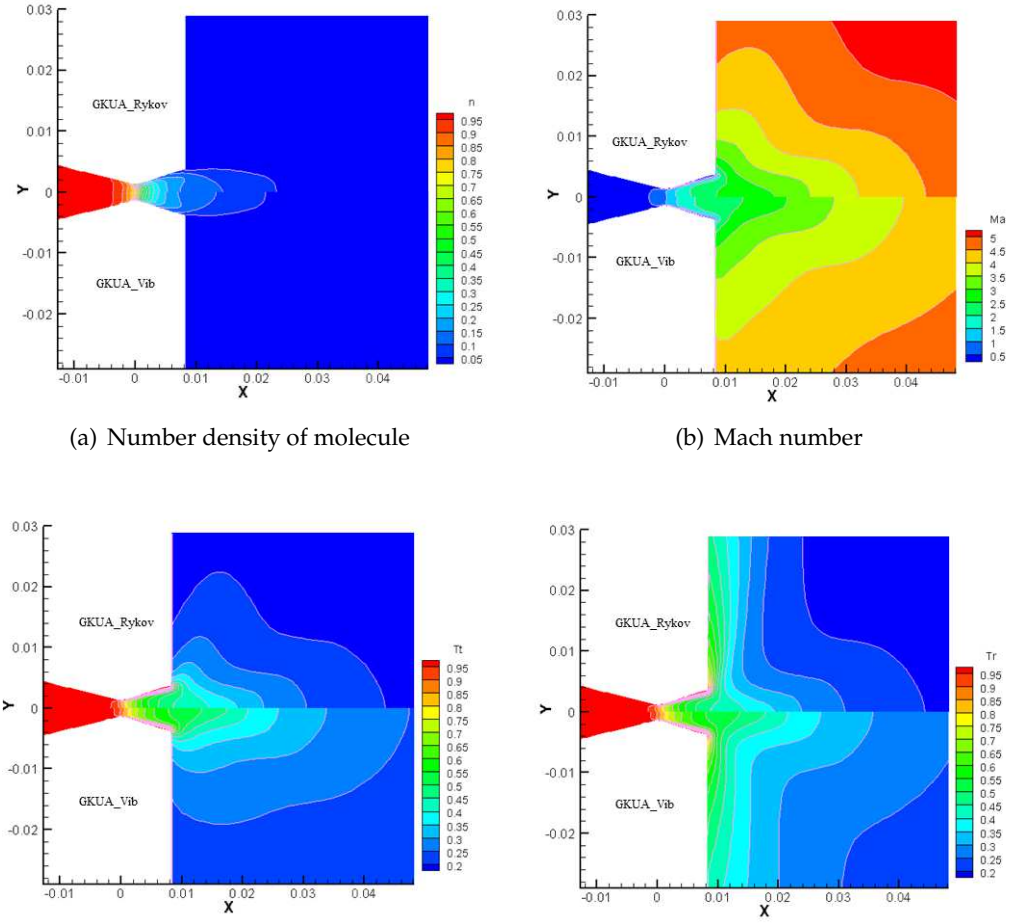

(a) Number density of molecule

(b) Mach number

(c) Translational temperature

(d) Rotational temperature

Figure 27: Comparison of GKUA results between Boltzmann model equation with vibrational energy excitation and Rykov model with rotational energy excitation.

and the Mach number will decrease. As can be seen from Fig. 26(a), the contour distributions of molecular number density obtained by the two models are basically in good agreement. It can be seen from Fig. 26(b) and (c) that there are great differences between the two models in the contour distributions of translational temperature and Mach number, which confirms that the internal energy excitation will affect the macroscopic flow parameter distributions and structure of the flow field.

Fig. 27 shows the comparison between the calculation results of GKUA based on Rykov model considering rotational energy excitation (represented by "GKUA_Rykov" in the figure) and the calculation results of Boltzmann model equation unified algorithm considering vibrational energy excitation in this paper (represented by "GKUA_Vib" in

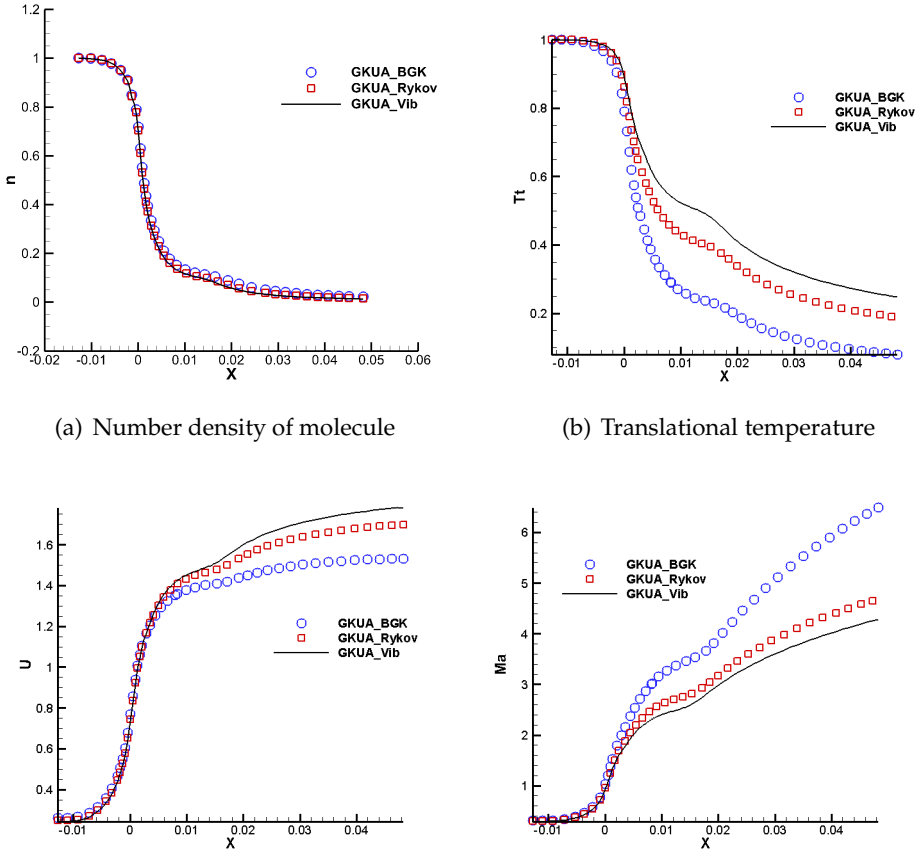

(a) Number density of molecule

(b) Translational temperature

(c) Axial velocity

(d) Mach number

Figure 28: Axis distributions of macroscopic flow parameters under the three models.

the figure). As can be seen from Fig. 27(a), the contour distributions of molecular number density obtained by the two models are basically in good agreement. As can be seen in Fig. 27(b), there are some differences in the contour distributions of Mach number obtained by the two models, and the Mach number obtained by the vibrational energy model is smaller than that obtained by the rotational energy model. As can be seen from Fig. 27(c) and (d), the contour distributions of translational temperature and rotational temperature obtained by the two models have the same structure, but there are some differences. The reason is that part of the vibrational energy is converted into rotational energy, so the rotational temperature and translational temperature of the vibrational energy model are higher than those of the rotational energy model.

Fig. 28 shows the distributions of macroscopic flow parameters along the axis considering the non-equilibrium effects of translational energy, rotational energy and vibration

energy under different kinetic models. As can be seen from Fig. 28(a), the axis distributions of the molecular number density under the three models are in good agreement, which is the same as the theoretical analysis, verifying the reliability of the results. As can be seen in Fig. 28(b), the translational temperature obtained by the vibrational energy model is the highest, followed by the rotational energy model and the lowest by the simple gas model. Fig. 28(c) shows that the axial velocity obtained by the vibrational energy model is the highest, followed by the rotational energy model and the lowest by the simple gas model. Fig. 28(d) shows that the Mach number obtained by the simple gas model is the highest, followed by the rotational energy model and the vibrational energy model. The Mach number at the axis is defined as $Ma=\frac{U}{\sqrt{\gamma T_t/2}}$. Compared with the simple gas model, considering the rotational energy/vibrational energy excitation, the translational temperature and axial velocity will increase, and the Mach number will decrease. Therefore, the following conclusions can be drawn: The influence of internal energy excitation on the temperature of the internal and external mixed flow field of the engine is much greater than its influence on the axial velocity, that is, the influence of internal energy excitation in the process of internal and external mixed flow mainly lies in the mutual transformation of internal energy itself rather than the transformation of kinetic energy.

4 Conclusion

By introducing the Larsen-Bergnakke model of DSMC method, the rotational energy and vibrational energy are treated as continuously distributed energy modes, and a unified algorithm for Boltzmann model equation of polyatomic gas is developed considering the excitation of vibrational energy. The algorithm is verified by using the polyatomic gas flow problem considering vibrational energy excitation, and then the internal and external mixed flow field analysis is carried out on the nozzle of 25N attitude control engine. The evolution law of the internal and external mixed flow field at different times, the evolution of the velocity distribution function at different points along the axis of the flow field, and the comparison among the simple gas model, the rotational energy model and the vibrational energy model are analyzed. According to the analysis, the internal energy excitation model should be considered instead of the simple gas model when the problem is related to high temperature environment. It is considered that the influence of internal energy excitation mainly lies in the mutual conversion of internal energy itself rather than the conversion with kinetic energy. When the problem under study involves a highly rarefied environment, the simple gas model should be used instead of the internal energy excitation model. For the in-orbit spacecraft engine internal and external mixed flow, the nozzle is in continuum and near-continuum flow regimes with high temperature and pressure, so the internal energy excitation model should be used. The temperature in the external field region is low and highly rarefied, and the simple gas model can be used.

Acknowledgments

This work is supported by the National Natural Science Foundation of China (12332013). The authors are thankful to the editors and reviewers for their valuable comments and suggestions, which greatly improved the quality of the manuscript.

References

[1] N. A. Brykov, V. N. Emelyanov, A. G. Karpenko and K. N. Volkov, Flows of real gas in nozzles with unsteady local energy supply, Computers and Mathematics with Applications, 81 (2021), 702-724.
[2] J. Gomez and R. Groll, Pressure drop and thrust predictions for transonic micronozzle flows, Physics of Fluids, 28 (2016), 022008.
[3] Z. H. Li, Z. H. Li, J. L. Wu and A. P. Peng, Coupled Navier-Stokes/direct simulation Monte Carlo simulation of multicomponent mixture plume flows, Journal of Propulsion and Power, 30 (2014), 672-689.
[4] D. B. Kanipe, Plume flowfield jet interaction effects on the space-shuttle orbiter during entry, Journal of Spacecraft and Rockets, 20 (1983), 351-355.
[5] A. L. Garsia, J. B. Bell, W. Y. Crutchfield and B. J. Alder, Adaptive mesh and algorithm refinement using direct simulation Monte Carlo, Journal of Computational Physics, 154 (1999), 134-155.
[6] H. A. Carlson, R. Roveda, I. D. Boyd and G. V. Candler, A hybrid CFD-DSMC method of modeling continuum-rarefied flows, 42nd AIAA Aerospace Sciences Meeting and Exhibit, (2004), 1180.
[7] T. E. Schwartzentruber, L. C. Scalabrin and L. D. Boyd, Hybrid particle-continuum simulations of nonequilibrium hypersonic blunt-body flowfields, Journal of Thermophysics and Heat Transfer, 22 (2008), 29-37.
[8] J. M. Burt and I. D. Boyd, A hybrid particle approach for continuum and rarefied flow simulation, Journal of Computational Physics, 228 (2009), 460-475.
[9] S. Liu, P. Yu, K. Xu and C. W. Zhong, Unified gas-kinetic scheme for diatomic molecular simulations in all flow regimes, Journal of Computational Physics, 259 (2014), 96-113.
[10] J. N. Zeng, Q. Li and L. Wu, Kinetic modeling of rarefied molecular gas dynamics, Acta Aerodynamica Sinica, 40 (2022), 1-30.
[11] Z. H. Li and H. X. Zhang, Study on gas kinetic unified algorithm for flows from rarefied transition to continuum, Journal of Computational Physics, 193 (2004), 708-738.
[12] J. L. Wu, Z. H. Li, A. P. Peng and X. Y. Jiang, Numerical Study on Rarefied Unsteady Jet Flow Expanding into Vacuum Using Gas-kinetic Unified Algorithm, Computers and Fluids, 155 (2017), 50-61.
[13] F. Li, Z. H. Li, X. Y. Jiang, W. Q. Hu, Z. H. Li and W. Q. Luo, Gas-kinetic unified algorithm for two-dimensional planar and axisymmetric nozzle flows, International Journal for Numerical Methods in Fluids, 95 (2023), 1617-1638.
[14] K. Xu and J. C. Huang, A unified gas-kinetic scheme for continuum and rarefied flows, Journal of Computational Physics, 229 (2010), 7747-7764.
[15] C. Liu, K. Xu, Q. Sun and Q. Cai, A unified gas-kinetic scheme for continuum and rarefied flows IV: Full Boltzmann and model equations, Journal of Computational Physics, 314 (2016), 305-340.

[16] G. Lim, Y. J. Zhu and K. Xu, High-Order Unified Gas-Kinetic Scheme, Communications in Computational Physics, 32 (2022), 951-979.
[17] Z. L. Guo, K. Xu and R. J. Wang, Discrete unified gas kinetic scheme for all Knudsen number flows: Low-speed isothermal case, Physical Review E, 88 (2013), 033305.
[18] Z. L. Guo, R. J. Wang and K. Xu, Discrete unified gas kinetic scheme for all Knudsen number flows. II. Thermal compressible case, Physical Review E, 91 (2015), 033313.
[19] Z. H. Li, A. P. Peng, Q. Ma, L. N. Dang, X. W. Tang and X. Z. Sun, Gas-kinetic unified algorithm for computable modeling of Boltzmann equation and application to aerothermodynamics for falling disintegration of uncontrolled Tiangong-No.1 spacecraft, Advances in Aerodynamics, 1 (2019), 1-21.
[20] Z. H. Li and H. X. Zhang, Gas-kinetic numerical studies of three-dimensional complex flows on spacecraft re-entry, Journal of Computational Physics, 228 (2009), 1116-1138.
[21] F. Fei, J. Zhang, J. Li and Z. H. Liu, A unified stochastic particle Bhatnagar-Gross-Krook method for multiscale gas flows, Journal of Computational Physics, 400 (2020), 108972.
[22] Y. J. Zhu, C. Liu, C. W. Zhong and K. Xu, Unified gas-kinetic wave-particle methods. II. Multiscale simulation on unstructured mesh, Physics of Fluids, 31 (2019), 067105.
[23] X. J. Yang, C. Liu, X. Ji, W. Shyy and K. Xu, Unified Gas-Kinetic Wave-Particle Methods VI: Disperse Dilute Gas-Particle Multiphase Flow, Communications in Computational Physics, 31 (2022), 669-706.
[24] C. S. Wang, The heat conductivity and viscosity of poly-atomic gases, Studies in Statistical Mechanics, 2 (1964).
[25] T. F. Morse, Kinetic Model for Gases with Internal Degrees of Freedom, Physics of Fluids, 7 (1964), 159-169.
[26] V. A. Rykov, Model Kinetic Equation of a Gas with Rotational Degrees of Freedom, Fluid Dynamics, 10 (1975), 959-966.
[27] L. H. Holway, New Statistical Models for Kinetic Theory: Methods of Construction, Physics of Fluids, 9 (1966), 1658-1673.
[28] A. P. Peng, Z. H. Li, J. L. Wu and X. Y. Jiang, Validation and analysis of gas-kinetic unified algorithm for solving Boltzmann model equation with vibrational energy excitation, Acta Physica Sinica, 66 (20) (2017), 204703.
[29] M. Liu, X. Zhang, G. Zhang and Y. Chen, Study on micronozzle flow and propulsion performance using DSMC and continuum methods, Acta Mechanica Sinica, 22 (2006), 409-416.